

**TESTING, INSTALLATION AND DEVELOPMENT OF HARDWARE  
AND SOFTWARE COMPONENTS FOR THE FORWARD PIXEL  
DETECTOR OF CMS**

by

**Carlos Andrés Flórez Bustos**

A thesis submitted in the fulfillment of the requirements for the degree of

**MASTER OF SCIENCE**  
in  
**PHYSICS**

UNIVERSITY OF PUERTO RICO  
MAYAGÜEZ CAMPUS  
2007

Approved by:

\_\_\_\_\_  
Angel López, PhD  
President, Graduate Committee

\_\_\_\_\_  
Date

\_\_\_\_\_  
Juan Eduardo Ramírez, PhD  
Member, Graduate Committee

\_\_\_\_\_  
Date

\_\_\_\_\_  
Esoy Velázquez, PhD  
Member, Graduate Committee

\_\_\_\_\_  
Date

\_\_\_\_\_  
Paul Castillo, PhD  
Representative of Graduate Studies

\_\_\_\_\_  
Date

\_\_\_\_\_  
Hector Jimenez, PhD  
Chairperson of the Department

\_\_\_\_\_  
Date

## **Abstract**

The LHC (Large Hadron Collider) will be the particle accelerator with the highest collision energy ever. CMS (Compact Muon Solenoid) is one of the two largest experiments at the LHC. A main goal of CMS is to elucidate the electroweak symmetry breaking and determine if the Higgs mechanism is responsible for it. The pixel detector in CMS is the closest detector to the interaction point and is part of the tracker system. This thesis presents four different projects related to the forward pixel detector, performed as part of the testing and development of its hardware and software components. It presents the methods, implementation and results for the data acquisition and installation of the detector control system at the Meson Test Beam Facility of Fermilab for the beam test of the detector; the study of the C.A.E.N power supply and the multi service cable; the layout of the test stands for the assembly of the half-disk and half-service cylinder and the development of a software interface to the data acquisition of the detector control system.

## **Resumen**

El LHC (Large Hadron Collider) será el colisionador de partículas de más alta energía que se halla construido. CMS (Compact Muon Solenoid) es uno de los detectores más grandes en el LHC. El propósito fundamental de CMS es elucidar el rompimiento de la simetría electrodébil y determinar si el bosón de Higgs es responsable de este rompimiento. El detector de píxeles es un componente del sistema que mide las trayectorias en CMS y es el detector más cercano al punto de colisión. Esta tesis presenta cuatro proyectos diferentes realizados como parte de las pruebas de la instrumentación y el desarrollo de programas para la lectura de datos del detector de píxeles. Este trabajo describe la metodología y los resultados empleados en la adquisición de datos y en la instalación del sistema de control para el detector en las pruebas realizadas en las instalaciones de Fermilab; el estudio de la fuente de voltaje C.A.E.N y del cable usados para proveer altos y bajos volates al detector; la instalación de un laboratorio para realizar las pruebas y ensamblaje de los medios-discos y del cilindro de servicio; y el desarrollo de una interfase de “software” para la adquisición de medidas de temperatura.

Copyright © 2006

By

Carlos Andrés Flórez Bustos

## **Dedictory**

To my best friends, who always believed in me

God, my father, my mother, my sister, my niece, Yuri Galindo and Richard Pérez

## **Acknowledgment of the Forward Pixel Collaboration Group**

I would like to thank all those who helped me with this work. Thank you for all the help, the support and for teaching me how real physics is done.

I want to mention specially Dr. Ricardo Vasquez Sierra, a postdoctoral researcher from the University of California who has been a good friend and the most important collaborator during my time at Fermilab. I will be thankful forever.

This work could not have been done without the collaboration of the following people:

- Professor Angel López who taught all the physics behind each project and helped me to be a better physicist and a better human being. I will be thankful forever.
- Dr. Kwan who trusted in me and gave me a hand when I needed most.
- Dr. Christian Veelken who fielded thousands of my questions
- Dr. Lorenzo Uplegger who saved my life at least ten times.
- Marcos Turqueti who gave me a hand when I needed it.

Since this thesis consists of four different projects, I want to give credit to the people that participated in each project separately.

## 1. Forward Pixel Beam Test

This project had the participation from people of different institutions, several universities from the USA, the INFN of Italy and an undergraduate summer student from Scotland.

- A. DCS Installation: Prof. Charles Newsom (University of Iowa), Dr. Christian Veelken (Postdoctoral researcher from the University of California, Davis), Pedro Titto (Graduate Student from the University of Puerto Rico) and Neal Kemp (undergraduate summer student from Scotland). The leaders of this project were Prof. Newsom and Dr. Christian Veelken. I would like to thank Prof. Newsom for all the things that he taught me and for his friendship at that time. Thanks to Dr. Veelken for his help, for his corrections to my work and Figure 4-2. Figures 4-3, 4-4, 4-5, 4-6, 4-7, and 4-8 were created by Prof. Newsom, Neal Kemp and myself. Thank you to Neal Kemp and Pedro Titto for the time that we spent together on the project.
- B. Data Acquisition of the beam test: The leadership of the data acquisition and analysis of the beam test data was exercised by physicists from the INFN from Italy (Luigi Moroni, Dario Menasce and Daniele Pedrini). The shifters that participated collecting data were: Pedro Titto, Prof. Charles Newsom, Dr. Lorenzo Uplegger (Fermilab), Max Bunce (Graduate student from the University of Colorado at Boulder), Silvia Taroni (Graduate student from the University of Milan), Francesca Valsecchi (Graduate student from Northwestern University) and Neal Kemp.

## **2. C.A.E.N. SY2527 Power Supply and MSC Cable**

I had the opportunity to work on this project with Prof Angel Lopez, Prof Charles Newsom and Dr. Lalith Perera (postdoctoral researcher from University of Iowa). Professor Lopez helped me in the physics analysis and to perform the measurements for the high voltage test. Dr. Perera designed the dynamic circuit used to perform the low voltage test and measured the capacitance values of the MSC cable.

## **3. Test Stand for the Partial Forward Pixel Detector**

The leader of this work was Mauro Dinardo (Postdoctoral researcher from University of Colorado at Boulder). Max Bunce also joined our group. Thanks to Dr. Dinardo for the pictures and Figure 5-17. I would like to thank the technicians from Sidet for all their collaboration, especially Bert Gonzalez, Steve Jakabowski and Ken Shultz.

## **4. DCS to FEC interface Software**

Thank you Prof. López, Dr. Veelken, Souvik Das (Graduate student from Cornell University) and Karl Ecklund (Prof. from University of Buffalo) for your help during this job, especially Prof. López and Dr. Veelken.

Finally I want to thank Dr. Sudhir Malik, Dr. Michael Eads, engineer Sergey Los and Mr. Erik Spencer for their help and explanations. Thank you Sergey for Figure 2-9.

## Table of Contents

Abstract .....	ii
Resumen .....	iii
Dedicatory .....	iv
Acknowledgments for the Forward Pixel Collaboration .....	v
Table of Contents .....	viii
Tables list .....	xii
Figures list .....	xiii
1. Introduction .....	1
1.1 Basic Concepts in Particle Physics .....	1
1.2 The LHC .....	2
1.2.1 LHC Physics Potential .....	2
1.2.1.1 The Higgs Boson .....	2
1.2.1.2 Supersymmetry Theory .....	3
1.2.1.3 The Big Bang .....	4
1.2.2 Performance .....	5
1.2.2.1 Beam Distribution .....	5
1.2.2.2 Goals .....	6
1.2.3 The CMS Experiment .....	7
1.2.3.1 The CMS Detector .....	7
1.2.3.2 Magnet Features .....	9
1.2.3.3 The Muon System .....	9



1.2.3.4	Calorimeters .....	10
1.2.3.5	The Tracker System.....	11
2.	Previous Work .....	12
2.1	Pixel Detectors .....	12
2.1.1	The p-n Junction .....	12
2.2	CMS Pixel System .....	15
2.3	The Forward Pixel Detector .....	16
2.3.1	System Readout for the Fpix .....	20
3.	Objectives .....	22
3.1	Forward Pixel Beam Test .....	22
3.2	C.A.E.N. SY2527 Power Supply and MSC Cable .....	22
3.3	Test Stand for the Partial Forward Pixel Detector .....	23
3.4	DCS to FEC interface Software .....	23
4.	Materials and Methods .....	24
4.1	Forward Pixel Beam Test .....	24
4.1.1	Test beam Facility .....	24
4.1.2	DCS and SMCS installation .....	26
4.1.3	Power distribution diagram .....	31
4.1.3.1	Data acquisition .....	33
4.2	C.A.E.N. SY2527 Power Supply and MSC Cable .....	34
4.2.1	C.A.E.N. components .....	34
4.2.2	CDF and MSC cables .....	35
4.2.3	Low voltage test setup .....	37

4.3	Test Stand for the Forward Pixel Detector.....	38
4.3.1	Half-disk cold box .....	39
4.3.2	Shunt Resistor for analog current measurement from the ROCs .....	42
4.3.3	Half-Service-Cylinder Cold Box .....	43
4.3	DCS to FEC interface Softwar.....	43
4.4.1	SOAP Message Format .....	46
4.4.2	Tasks of the PixelDCStoTrkFECDpInterface .....	46
4.4.3	Running XDAQ .....	47
5.	Results .....	49
5.1	Forward Pixel Beam Test .....	49
5.1.1	DCS Results .....	49
5.1.2	Test beam results .....	49
5.2	C.A.E.N. SY2527 Power Supply Test and MSC Cable .....	54
5.2.1	Low voltage results .....	54
5.2.1.1	Basic behavior of the power supply .....	54
5.2.1.2	Power supply response .....	58
5.2.1.2.1	Sag .....	60
5.2.1.2.2	Recovery times .....	60
5.2.1.2.3	Signals with capacitor .....	62
5.2.2	High voltage test .....	64
5.2.2.1	Spikes in the low voltage and high voltage output .....	65
5.2.3	High voltage and low voltage at the same time .....	65

5.3	Test Stand for the Partial Forward Pixel Detector .....	68
5.3.1	Cooling test and leakage current measurement .....	68
5.3.2	Half-service-cylinder Cold Box .....	69
5.4	DCS to FEC Interface .....	70
5.4.1	Interface Status .....	70
6.	Summary and Conclusions .....	74
6.1	Forward Pixel Beam Test .....	74
6.2	C.A.E.N. SY2527 Power Supply and MSC Cable .....	74
6.3	Test Stand for the Partial Forward Pixel Detector.....	75
6.4	DCS to FEC interface Software .....	75
	References .....	77

## Table List

<b>Tables</b>	<b>Page</b>
Table 1-1 CMS magnet features .....	9
Table 4-1 Description of the MSC cable .....	37
Table 5-1 Temperature data for the beam test in July, 2006 .....	50
Table 5-2 Temperature data for the beam test in July and August of 2006 .....	51
Table 5-3 Nitrogen Level at the test beam for the CMS Fpix detector in July and August of 2006 .....	52
Table 5-4 Examples of run conditions during some tests of a non irradiated production plaquette .....	54

## Figure List

Figure		Page
Figure 1-1	Signal of a Higgs boson with mass of $130 \text{ GeV}/c^2$ decaying to two photons .....	3
Figure 1-2	Signal of a Higgs boson with mass of $300 \text{ GeV}/c^2$ decaying to two tau ( $\tau\tau$ ) .....	5
Figure 1-3	LHC, SPS and SP at CERN laboratory .....	6
Figure 1-4.	CMS detector diagram .....	8
Figure 1-5	Coordinate system convention used for the CMS detector .....	9
Figure 1-6	Layout of one quarter of the CMS muon system for initial low luminosity running .....	10
Figure 2-1	p-n junction of an extrinsic semiconductor .....	13
Figure 2-2	Particle hitting a pixel sensor .....	14
Figure 2-3	CMS pixel detector geometry .....	16
Figure 2-4	One blade of the CMS Fpix detector .....	18
Figure 2-5	Mechanical structure of a half-disk of the CMS Fpix detector .....	18
Figure 2-6	Silicon sensor connected to the chip readout system (ROCs) using the bump bond technique .....	19
Figure 2-7	Fully instrumented and tested half-disk for the Fpix detector .....	19
Figure 2-8	Block diagram of pixel control and readout system .....	21
Figure 2-9	Adapter board for the CMS Fpix detector .....	21
Figure 4-1	Telescope used to test the CMS pixel detector, located at the test beam facility .....	25
Figure 4-2	Schematic diagram of the Siemens Modules distribution .....	28

Figure 4-3.	Front view of the DCS rack RR05 for the Fpix detector in the test beam Facility .....	29
Figure 4-4	Back view of the top half of the DCS rack RR05 for the Fpix detector in the test beam facility .....	30
Figure 4-5	Back view of the bottom half of the DCS rack RR05 for the Fpix detector in the test beam facility .....	30
Figure 4-6	Power routing diagram one for the DCS and SMCS systems at the test beam facility .....	31
Figure 4-7	Power routing diagram two for the DCS and SMCS systems at the test beam facility .....	32
Figure 4-8	Power routing diagram three for the DCS and SMCS systems at the test beam facility .....	32
Figure 4-9	Layout of the main mechanical section of the SY2527 mainframe .....	35
Figure 4-10	Cross section of the CDF cable .....	36
Figure 4-11	Cross section of the MSC cable .....	36
Figure 4-12.	Diagram of connections for the cable high voltage test .....	38
Figure 4-13	Assembly of the partial forward pixel detector .....	39
Figure 4-14	(a) Half-disk cold box and power supplies for the extension cable board. (b) High voltage power supply and test stand with computers to test and monitor the half-disk for the Fpix detector .....	40
Figure 4-15	Extension Cable Board to test the half-disk for the CMS Fpix detector .....	41
Figure 4-16	Chiller for the half-disk test of the CMS Fpix detector .....	42
Figure 4-17	Routing for the cooling lines of the half-disk test cold box for the CMS Fpix detector .....	42
Figure 4-18	Circuit diagram for the shunt resistor connection .....	43
Figure 4-19	Cold box and electronic devices for the Half-service-cylinder at Sidet .....	44
Figure 4-20	Flow of information and control in the pixel data acquisition system .....	45

Figure 4-21	XDAQ browser display which includes the PixelDCStoTrkFECDpInterface application .....	48
Figure 5-1	Nitrogen Level vs. Time .....	52
Figure 5-2	Efficiency study for different pixels of an irradiated detector .....	53
Figure 5-3	Active part of the circuit during the study of the basic behavior of the power supply .....	56
Figure 5-4.	Power supply driving voltage vs. current .....	57
Figure 5-5	Power supply driving voltage versus current for 2.5 and 1.75V nominal voltages, with the MSC cable .....	57
Figure 5-6	Curves for the low voltage test with the C.A.E.N. power supply .....	59
Figure 5-7	Sag vs. Current for different nominal voltages, with and without capacitor .....	60
Figure 5-8	Fast and slow recoveries for a circuit without capacitor, nominal voltage of 1.8V and 11 $\mu$ s pulse width .....	61
Figure 5-9	Fast recovery times vs current for a circuit without capacitor, nominal voltage of 1.8V and 11 $\mu$ s pulse width .....	62
Figure 5-10	Slow recovery time vs current for a circuit without capacitor, nominal voltage of 1.8V and 11 $\mu$ s pulse width .....	62
Figure 5-11	a) Signal without capacitor b) signal with capacitor of 13 $\mu$ F .....	63
Figure 5-12	High voltage tests with the plaquette IZM1 (1X2) .....	65
Figure 5-13	Spikes in the low voltage and high voltage power supply output .....	66
Figure 5-14	Diagram of the circuit used to test the 3 high voltage and low voltage channels at the same time .....	67
Figure 5-15	Two low voltages and one high voltage from one channel connected simultaneously using the CMS cable .....	67
Figure 5-16	Temperature vs. leakage current for each panel on the first half-disk of the Fpix detector .....	68

Figure 5-17	Fit for the leakage current on panel1 as a function of temperature .....	69
Figure 5-18	View upper half part of the PixelDCStoTrkFECDpInterface browser .....	70
Figure 5-19	Message sent from PixelDCSMessage to test the PixelDCStoTrkFECDpInterface .....	71
Figure 5-20	Debug output generated by the decoding of the SOAP message received from the PixelDCSMessage test application .....	72
Figure 5-21	Lower half of the webpage displayed by PixelDCStoTrkFECDpInterface application .....	73



## Chapter 1 - Introduction

### 1.1 Basic Concepts in Particle Physics

Elementary particle physics is a branch of physics that studies the basic constituents of matter and their interactions. Several elementary particles have been discovered. Their characteristics and the interactions between them are summarized in a physics model called the Standard Model (SM). In the SM, matter is composed of 12 elementary particles that are governed by Fermi statistics. This set of elementary particles is divided in two groups of leptons and quarks, six of each. The known interactions between particles are carried by another set of particles that follow Bose statistics. The SM model describes three kinds of interactions and their carriers which are: electromagnetic (photon), weak ( $Z^0$ ,  $W^+$ ,  $W^-$  bosons) and color (eight gluons). Gravitation is not included in the SM. On the other hand, the SM unifies the electromagnetic and the weak interactions into a single one called the electroweak interaction. This unification is based on postulating that the electroweak interaction satisfies a local gauge symmetry, i.e. a situation where the physics is invariant under a transformation which adds a phase to the matter fields, this phase being different at every point in space-time.

When the electroweak interaction was first proposed, it required that the four carriers be massless. The photon is a massless carrier, mediating electromagnetic interactions; but the same is not true with the weak interaction carriers. The fact that they have mass is an indication that the symmetry is broken in nature. However, the SM postulates that the symmetry is not broken by the interaction per se but rather by the ground state, or vacuum. This phenomenon is called “spontaneous symmetry breaking”. The SM postulates that there exists an additional interaction between all particles and a still unobserved field called the Higgs field which is the reason the ground state vacuum is not symmetric. When this additional interaction is added to the theory, it

is possible to accommodate electroweak intermediaries with mass. In addition, the matter particles themselves have a mass which springs essentially from the Higgs interaction. Intermediaries and matter particles with mass is what is observed experimentally. The SM with a Higgs boson is a theory which unifies the electromagnetic and weak interactions while being consistent with experimental observations. One of its great successes was an exact prediction of the masses of the weak intermediaries [1], a prediction which was made before they had been observed directly and which was verified by the experimental observations.

The indirect evidence for the Higgs boson is strong but its existence must, of course, be verified by direct observation. This is one of the main goals of experimental high energy physics today. Also, many variants of the Higgs scenario have been proposed for reasons which are not relevant to this discussion. The point is that it could be that there is a whole family of Higgs particles. It is important to determine the exact nature of the Higgs phenomenon.

## **1.2 The LHC**

The LHC (Large Hadron Collider) is a proton-proton collider that is being built at the European Center for Nuclear Research (CERN), at the border between Switzerland and France. Once the LHC reaches its design collision energy of 14TeV (7TeV per proton) beam, it will be the highest collision energy ever achieved at any particle accelerator.

### **1.2.1 LHC Physics Potential**

#### **1.2.1.1 The Higgs Boson**

In the LHC will be observed  $W$  and  $Z$  bosons and  $t$  quarks through their decays into leptons (muons and electrons). Events in the muon channels, such as  $W \rightarrow \mu \nu_\mu$ ,  $Z \rightarrow \mu^+ \mu^-$  and

$t\bar{t} \rightarrow W^+bW^-\bar{b} \rightarrow \mu\nu_\mu + X$  will be seen. A complete understanding of these events is important since they contain the biggest source of background for the Higgs boson search.

Muons will be one of the most important signals to study at the LHC. Two interesting decay modes where the Higgs boson could be found are  $ZZ$  and  $ZZ^*$  which decays into four charged leptons. A decay of the Higgs boson into four leptons  $H \rightarrow ZZ \rightarrow \ell^+\ell^-\ell^+\ell^-$  is expected if its mass is from 130 to 600 GeV/c<sup>2</sup> [1]. To search for the Higgs boson in a mass range below 130 GeV/c<sup>2</sup>, one has to use other decays channels such as  $\gamma\gamma$ ,  $b\bar{b}$  y  $\tau\bar{\tau}$ . However, these channels are difficult to study since a large background is present. Figure 1-1 shows the difficult task for a signal of a Higgs boson of 130 GeV/c<sup>2</sup> which decays to  $\gamma\gamma$ .

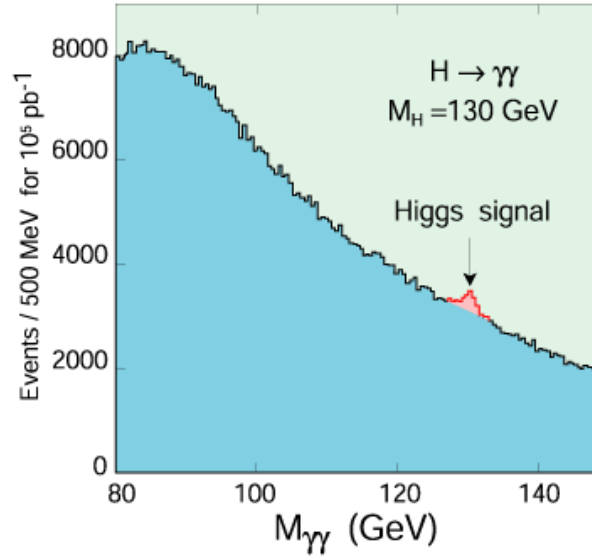


Figure 1-1. Signal of a Higgs boson with mass of 130 GeV/c<sup>2</sup> decaying to two photons.

### 1.2.1.2 Super Symmetry Theory

There is a suggested Super Symmetry (SUSY) theory which is an extension of the SM in which all four interactions are derived from a unique fundamental interaction. According to

SUSY, each particle has a supersymmetric partner. For fermions (particles with spin 1/2) there exist particles superpartners of spin 0 (boson). In this case, each superpartner is labeled adding a (s) before to the fermions name which is its superpartner (i.e. for the electron the superpartner is selectron). For the bosons (particles with integer spin) the particle superpartner is a fermion which is labeled adding the termination (ino) to the name of the particle (i.e. for the photon the superpartner is photino). SUSY incorporates the gravitational interaction. A boson called graviton is presumed to be responsible of the interaction. According to SUSY the superpartner particles have not been detected yet because their mass is too large. It assumes the existence of superpartners with TeV scale masses.

For the Higgs boson, the MSSM (Minimal Supersymmetric Standard Model) increases the number of Higgs bosons to five, two charged  $H^\pm$  and three neutrals  $h^0, H^0$  and  $A^0$  which can decay in different modes  $e^\pm, \mu^\pm, \tau^\pm$  and jets in the final states. Figure 1-2 shows the mass reconstruction for Higgs bosons decaying in  $\tau\tau$ .

### **1.2.1.3 The Big Bang**

By colliding protons at high energies we can recreate the earliest moments of the beginning of our Universe. The Big-Bang theory was postulated in the 1929. It proposes that, at the beginning of time, the Universe was in a state of incredibly high density and high temperature. The average energy per particle was very high. Since then the Universe has been expanding and cooling down. The LHC is in some way a time machine since it recreates the energy conditions that were present in the early universe. It is believed that the discoveries at the LHC will allow us to understand better the evolution of the universe.

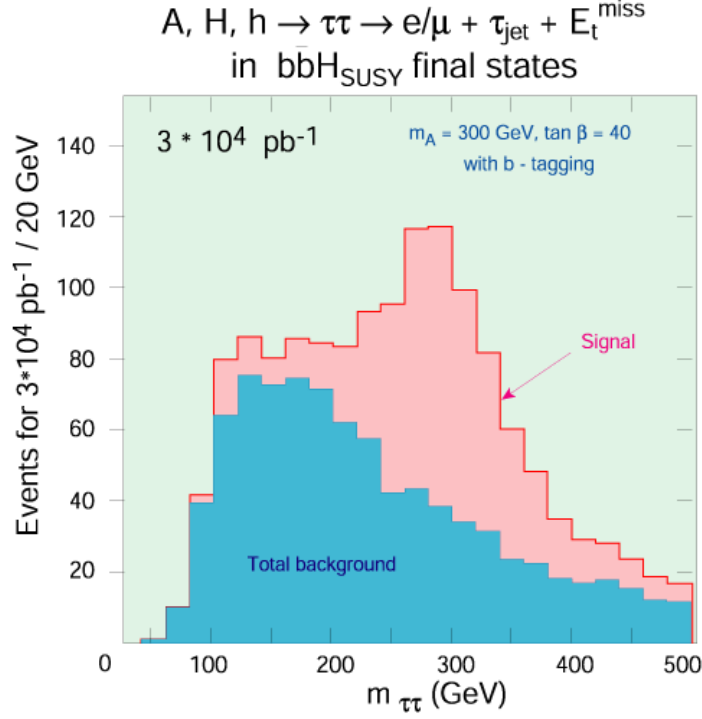


Figure 1-2. Signal of a Higgs boson with mass of  $300 \text{ GeV}/c^2$  decaying to two tau ( $\tau\tau$ ).

## 1.2.2 Performance

The LHC is located in a 27Km circumference tunnel located 50 to 150 meters underground [2]. Its nominal luminosity is  $10^{34} \text{ cm}^{-2} \text{ s}^{-1}$ . The LHC consists of a set of 1232 superconducting dipole magnets cooled down by liquid helium. It has radio frequency accelerating cavities providing a kick to the protons passing through, increasing their energy in 0.5MeV each turn.

### 1.2.2.1 Beam Distribution

A single proton will take around  $90\mu\text{s}$  to travel once around the collider. The protons will be bunched and will have a time difference of 25 ns between them. The bunches are formed in the 26GeV Proton Synchrotron (PS) with the correct 25ns spacing. The beam is subsequently

accelerated to 450GeV in the Super Proton Synchrotron (SPS) and transferred to the LHC (Figure 1-3).



Figure 1-3. LHC, SPS and PS at CERN laboratory

#### **1.2.2.2 Goals**

Is the SUSY model true? Does the Higgs boson exist? These are some of the questions that we intend to answer. Four experiments CMS, ATLAS, LHCb and ALICE are being constructed at the LHC aiming to answer some or all of these questions. In spring 2008 the LHC is scheduled to start running. This initial run will be an engineering run or pilot run and its main purpose will be to calibrate the LHC and the detectors. After this calibration process the first physics run will take place. It is envisioned to keep the experiments running for a few years. Then the experiments will be upgraded and are expected to be running for 10 more years with a higher luminosity and improved detectors.

### **1.2.3 The CMS Experiment**

The CMS experiment is one of the two largest experiments at the LHC. This experiment has been constructed with the participation of 60 countries including the United States. Forty eight universities from the USA, including the University of Puerto Rico, have been working together in the detector construction and software development for simulation, data acquisition, hardware control and data analysis for the CMS detector. The University of Puerto Rico has been actively working on the hardware, software and simulation level for the forward pixel detector. The primary goal of CMS is to elucidate the nature of the electroweak symmetry breaking for which the Higgs mechanism is presumed to be responsible [3].

#### **1.2.3.1 The CMS Detector**

With a total weight of 12500 tons, a length of 21.6m and a diameter of 14.6m the CMS detector is one of the two largest detectors at the LHC. Superconducting technology for the magnets will make possible a 4T magnetic field. A diagram of the CMS detector and its components is shown in Figure 1-4. The coordinate system convention used for the CMS detector is shown in Figure 1-5.

In CMS, at the nominal luminosity, is expected a bunch crossing frequency of 40 MHz with an average of  $\sim 15$  pp interactions per crossing. A first level trigger of 30 MHz will make an initial filter for the events, searching for interactions of muons, electrons, photons and missing energy. A second trigger called the high level trigger will be applied to the remaining events after the first level trigger is applied. This high level trigger will perform a more detailed selection of events applying stricter criteria. The high level trigger operates at an input frequency of 100 kHz and outputs at 100 Hz.

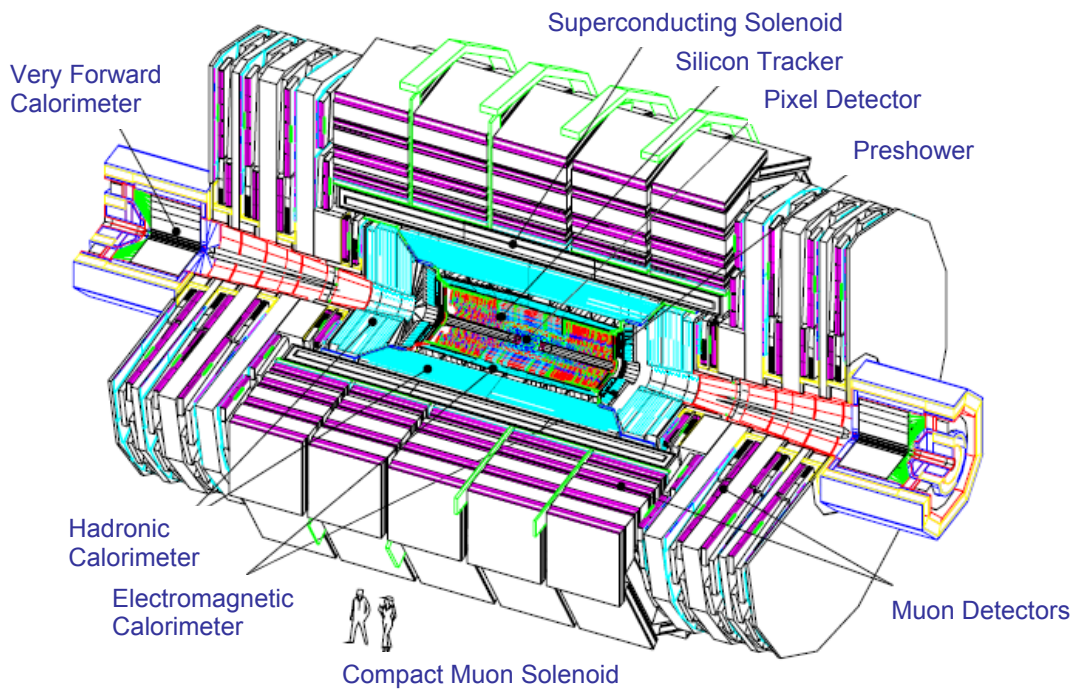


Figure 1-4. CMS detector diagram.

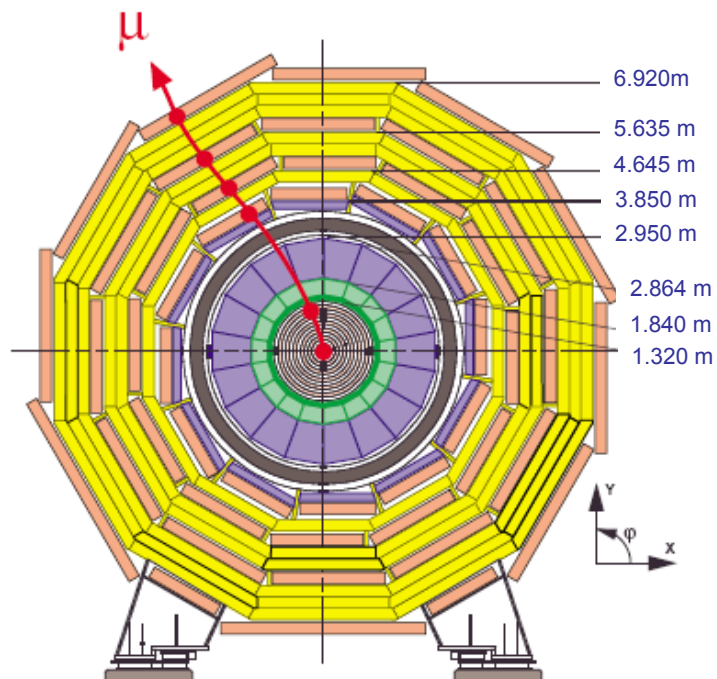


Figure 1-5. Coordinate system convention used for the CMS detector.



### 1.2.3.2 Magnet Features

The magnetic field strength and its precise control are of fundamental importance for the CMS detector. The CMS detector has a superconducting solenoid magnet made of high-purity aluminum-stabilized conductor. With 2168 turns, a length of 12.9 m and an inner bore of 5.9 m, the CMS magnet can produce a magnetic field of 4T which is required to perform a precise measurement of muons and other charged particle momenta. The most important features of the CMS magnet are listed in Table 1-1.

### 1.2.3.3 The Muon System

Three types of gaseous detectors will be used for the muon system: drift tube (DT) chambers, cathode strip chambers (CSC) and resistor plate chambers (RPC). The objective of this system is to identify muons of low and high energies and measure their momentum. The layout of one quarter of the CMS muon system for the initial low luminosity [3] run is shown in Figure 1-6.

Table 1-1 – CMS magnet features

Field	4T
Inner Bore	5.9m
Length	12.9m
Number of Turns	2168
Current	19.5kA
Stored energy	2.7GJ
Hoop stress	64 atm

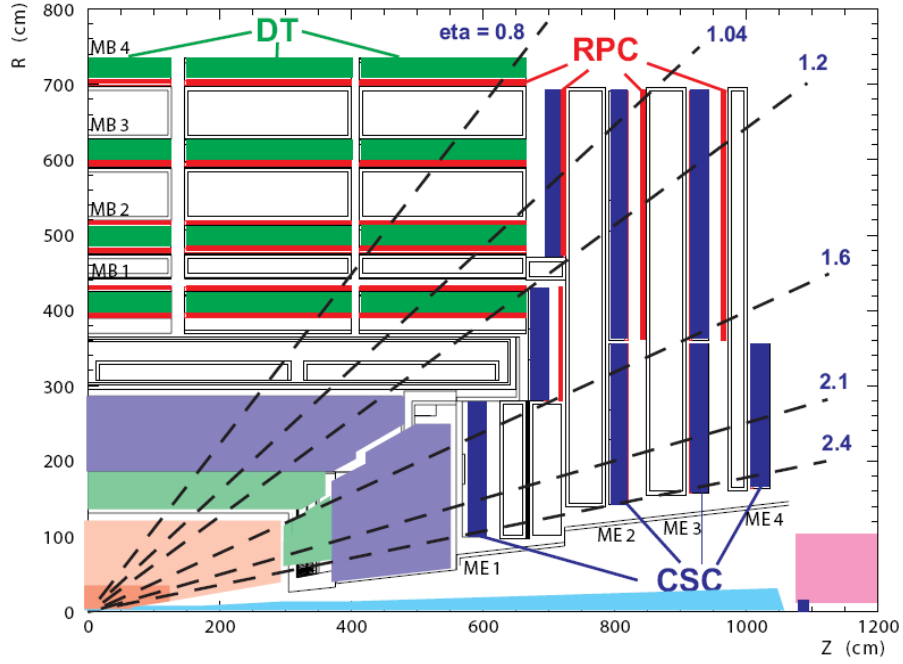


Figure 1-6. Layout of one quarter of the CMS muon system for initial low luminosity running.

DT chambers were used in the barrel region ( $|\eta| < 1.2$ ) where the muon rate is low, the residual magnetic field in the chambers is low, and the neutron induced background is small [3]. CSC chambers were used for the two endcaps ( $|\eta| < 2.4$ ) where the muon rate, the background and the magnetic field are high. RPCs are used at both regions (barrel and endcaps).

### 1.2.3.4 Calorimeters

The calorimeter system consists of electromagnetic and hadron calorimeters. The electromagnetic calorimeter (ECAL) consists of 61200 tungstate crystals ( $PbWO_4$ ) [3]. The ECAL is a compact detector located inside the solenoid, with inner radius of 1.29 m at the barrel section and two endcaps at a distance of 3.14 m from the interaction point. Since the ECAL is exposed to a high radiation dose, the radiation resistant  $PbWO_4$  crystals are used.

Most of the Hadron Calorimeter (HCAL) is located inside the magnetic solenoid. One important task of the HCAL is to improve the energy resolution and to provide a good hermeticity for the measurement of missing energy [3]. Outside the magnetic solenoid, a layer of scintillators known as the Hadron Outer detector (HO), complement the HCAL system.

### **1.2.3.5 The Tracker System**

The tracker system consists of two detectors: the pixel detector and the silicon strips. The pixel detector features will be detailed in the next chapter.

The silicon strip detector has portions in the barrel and others in the forward region of CMS. The barrel region is divided in two parts: the inner and outer barrel, in which the silicon microstrip detectors are placed at  $r$  between 20 and 110 cm [3]. The forward region consists of endcaps divided into two sets of disks: 9 Tracker End Caps (TEC) and 3 Tracker Inner Disks (TID).

## **Chapter 2 - Previous Work**

### **2.1 Pixel Detectors**

Hybrid pixel detectors are new in high energy physics. Some previous experiments such as Delphy, WA92 and WA98 have used pixel detectors. They have been in research and development for many years and they share many characteristics with silicon strip detectors which have been used successfully in several experiments. Three of the LHC experiments (ATLAS, ALICE and CMS) will attempt to use pixel detectors in the inner part of their tracker systems for reconstruction of primary and secondary vertices.

#### **2.1.1 The p-n Junction**

Silicon is one of the most used semiconductor materials in the development of electronic devices. The basic principle of a pixel detector is a p-n junction. In other words, a pixel detector is a special type of diode (pixel diode).

A p-n junction is generated when a piece of an extrinsic semiconductor doped as n type is joined together with a material doped as p type. An extrinsic semiconductor is made by adding impurities which alter the material properties. If the material is altered by adding electrons in it, it is known as n-doped material. If the material is altered by adding holes in it, it is known as p-doped material. Once the p-doped and n-doped parts are joined together a diffusion process will take place. Electrons will move into the p region and holes will move into the n region. Due to the diffusion process an excess of negative charge will be produced in the p region and an excess of positive charge will be produced into the n region creating an electric field [4] that counteracts the diffusion process (Figure 2-1). In Figure 2-1 the red rectangle marks the diffusion region, usually called the junction or depletion region, in the diode. In this region there are no available charge carriers since they have diffused away.

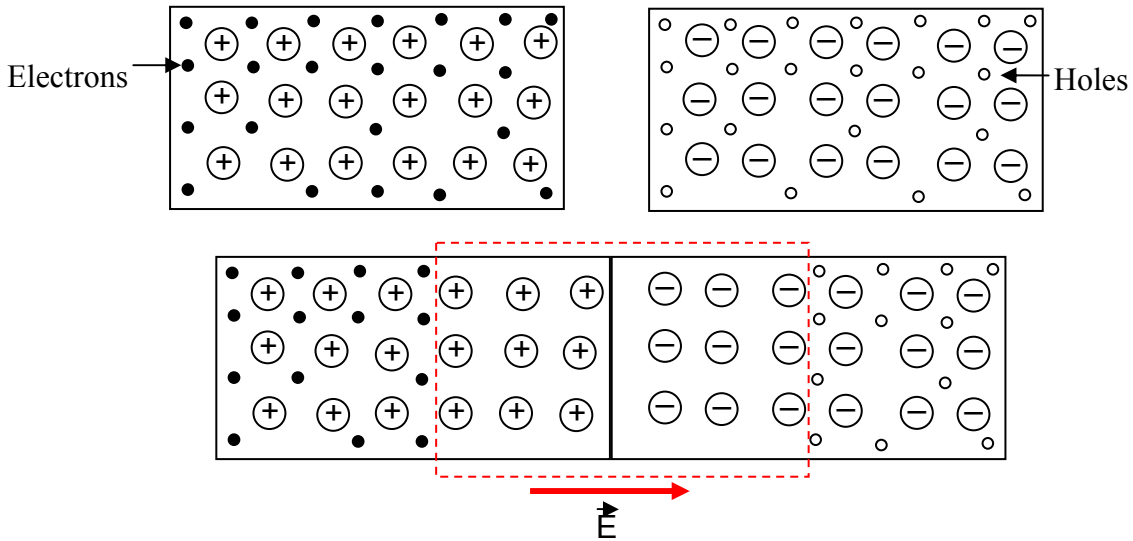


Figure 2-1. p-n junction of an extrinsic semiconductor.

When an external high energy charged particle traverses the depletion region, it creates hole-electron pairs by the process of ionization. These charge carriers separate under the influence of the electric field. They move freely through the depletion region because there are no other carriers of opposite sign with which to recombine. But this current dies quickly outside the depletion region due to recombination. In order to avoid this recombination, active detector diodes use a reverse voltage (called a bias voltage) in order to cause the depletion region to cover the complete volume of the diode. Thus the carriers generated by the ionization can be collected and detected outside the diode. Their presence is the signal of the passage of the high energy particle. The bias voltage causes a constant current (called a leakage current) to be established in the diode. The value of the bias voltage is very important. It must be large enough to cause effective depletion but as small as possible to minimize the leakage current

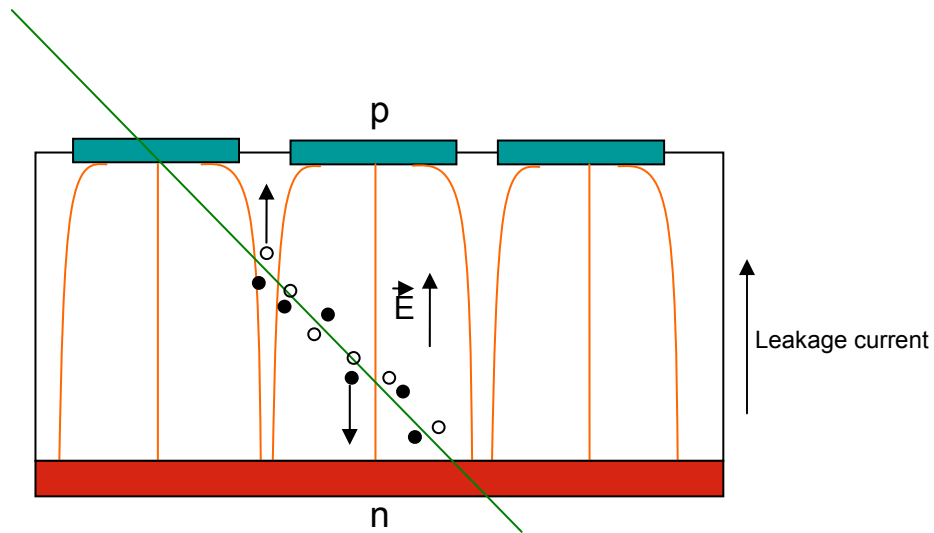


Figure 2-2. Particle hitting a pixel sensor.

Figure 2-2 shows an example of an ionizing particle passing through a pixel sensor creating electron-hole pairs. The connection to one side of the diode is divided into sections each of which makes up an independent detector channel. Except for cases of extremely non-normal incidence, the signal from this device will be collected in a limited number of channels and precise information about the position of the ionizing particle can be derived. The resolution of such a position measurement will, of course, depend crucially on the size of the connection structure.

This behavior is the functional basis of all semiconductor detecting devices including strips and pixels. The difference between them is the way that external circuits are connected to the diode. For strips the connector is rectangular with one dimension much longer than the other and the current can be extracted from the side. For pixels the connector is nearly square and the connection is perpendicular to the diode. Since the interest is for resolutions of the order of tens of micrometers, the main technical difficulty in developing pixels was a connection scheme of

such dimensions which could be made reliable. The solution to this problem is the “bump-bonding” technology which places a microscopic dot of conducting material on each pixel.

## 2.2 CMS Pixel System

At the LHC, one interesting topic of analysis will be b-jet reconstruction. The b-jets are generated by heavy particle decays. To be able to identify this type of decay and other kinds of events, the tracking system should be as close as possible to the interaction point. The CMS Silicon Pixel Detector is the closest detector to the interaction point, with about 66 million pixels each one with a rectangular shape of  $150\mu m \times 100\mu m$ . The pixel detector provides two or more hits per track, allowing the detection of secondary vertices generated by relatively long-lived particles such as b or c quarks or  $\tau$  leptons [5]. Due to the high luminosity at the LHC, the pixel detector will be an important component of the CMS detector for reconstruction of events with many tracks.

The pixel detector consists of three barrel layers located at mean radii of 4.4 cm, 7.3 cm and 10.2 cm, and two endcap disks (forward) assembled in a turbine-like geometry, extending from 6 to 15 cm in radius. Figure 2-3 shows the CMS pixel detector geometry. The three barrel layers have a length of 53 cm, and the endcap disks are placed at  $|z| = 34.5$  cm and 46.5 cm. The CMS pixel detector layers are composed of modular detector units of segmented sensor plates connected to a system of readout chips (ROC) using the bump bond technique. The bump bond is a  $25\mu m$  solder ball of Pb-Sn mixture.

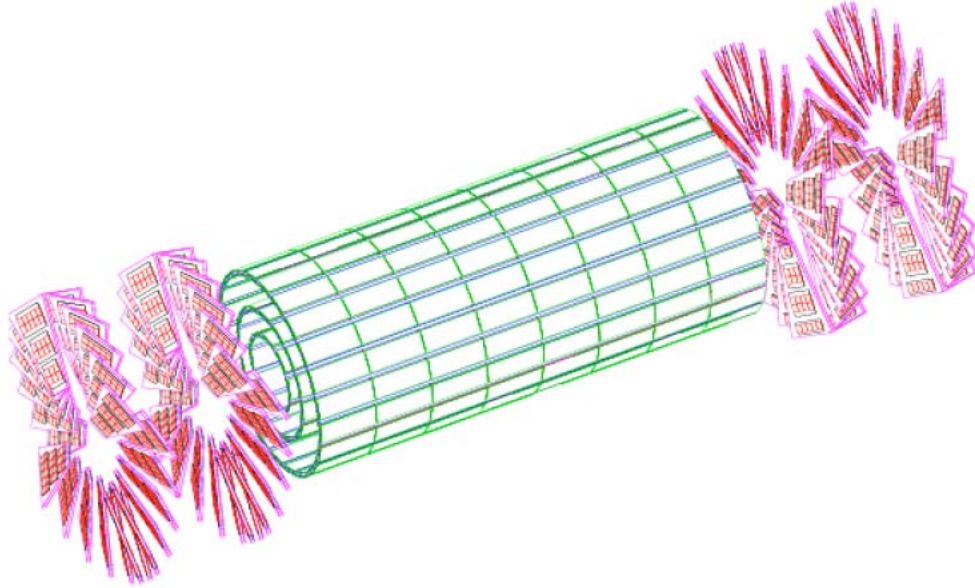


Figure 2-3. CMS pixel detector geometry.

The ROCs are connected to the Token Bit Manager (TBM) chip that performs the readout control and synchronizes the signals for the data collection process. Kapton cables connected to hybrid (digital and analog signals) circuits transmit the signals to and from the outer region of the pixel system where detector control chips and electro optical converters for optical signal transmission are located [6]. This communication process will be explained in section 2.3.1.

## 2.3 The Forward Pixel Detector

The Forward pixel detector (Fpix) is currently being built at different places in the United States. The final assembly and testing process is being performed at Fermilab National Accelerator Laboratory in Batavia, Illinois. Each disk of the Fpix includes 24 blades with two panels (Figure 2-4), one to each side of the blade, mounted over a mechanical structure frame with cooling channels running internally (Figure 2-5).

A panel is made up of 3 or 4 plaquettes of different sizes. A plaquette consists of a pixel sensor connected to a set of ROCs through bump bonds (Figure 2-6). The ROCs are mounted on



a Very High Density Interconnect (VHDI) that provides power, control and data connections. The VHDI is composed of a two-layer flexible printed circuit laminated on a  $300\mu m$  thick silicon plate. A High Density Interconnect (HDI) is used to connect the plaquettes on a 0.5 mm thick beryllium plate. The HDI is a three-layer flexible printed circuit used to transfer analog signals and digital control.

The blades are rotated  $20^\circ$  with respect to the beam direction in order to increase the probability of charge sharing between neighboring pixels which improves the position resolution. The forward pixel detector will be built in units of “half-disk” before final assembly in CMS. Two half-disks will be mounted on a “half-service-cylinder” which provides the structural support for the half-disks as well as the readout electronics and the power and cooling lines.

The C.A.E.N. SY2527 controller with the LV/HV A4603 module is the system that will provide the low voltage and high voltage for the Fpix detector. The prototype MSC (Multi Service Cable) distributes the low voltage and high voltage from the power supply to the half-service cylinder.

Figure 2-7 shows a fully instrumented and tested half-disk. At the time most of the work reported in this thesis was performed only prototype components existed which needed to be tested in order to arrive at the final design.

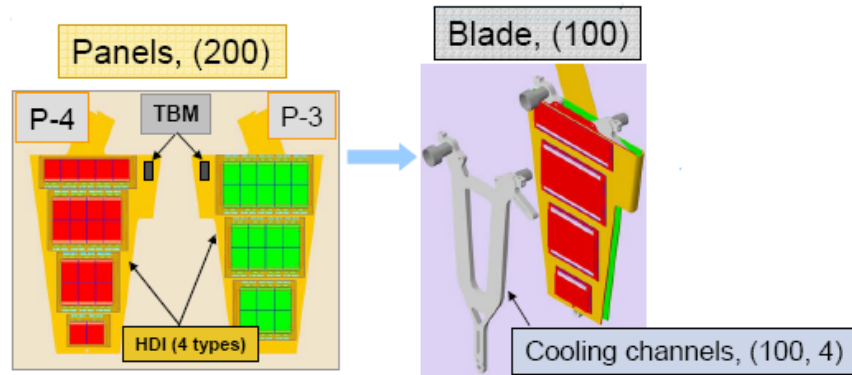


Figure 2-4. One blade of the CMS Fpix detector. Two panels are joined back to back to form a blade.

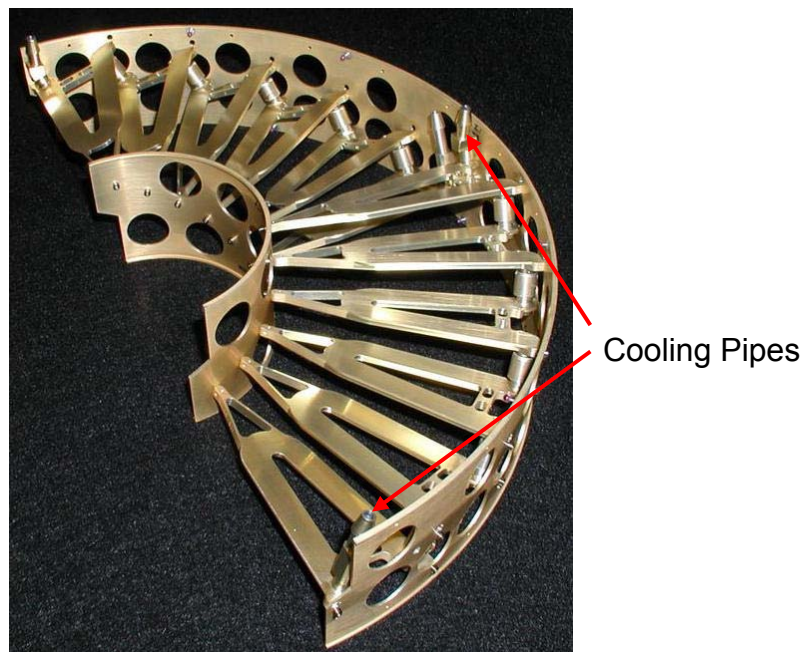


Figure 2-5. Mechanical structure of a half-disk of the CMS Fpix detector.

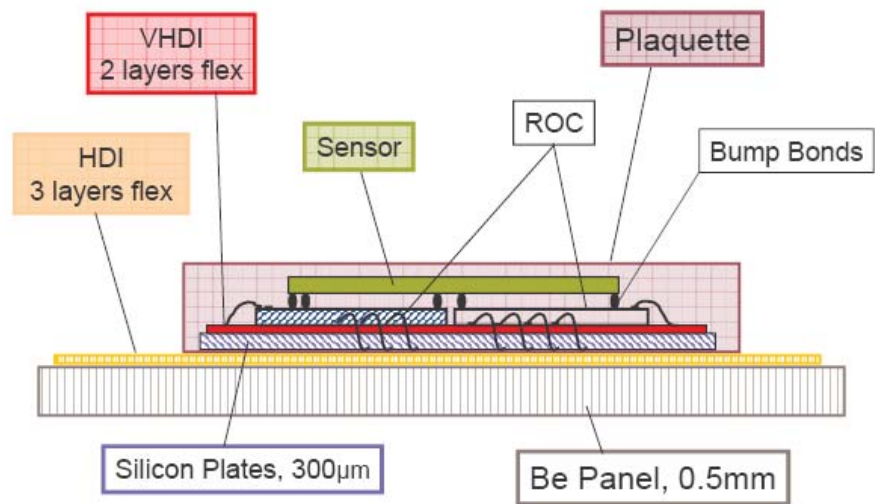


Figure 2-6. Silicon sensor connected to the chip readout system (ROCs) using the bump bond technique.

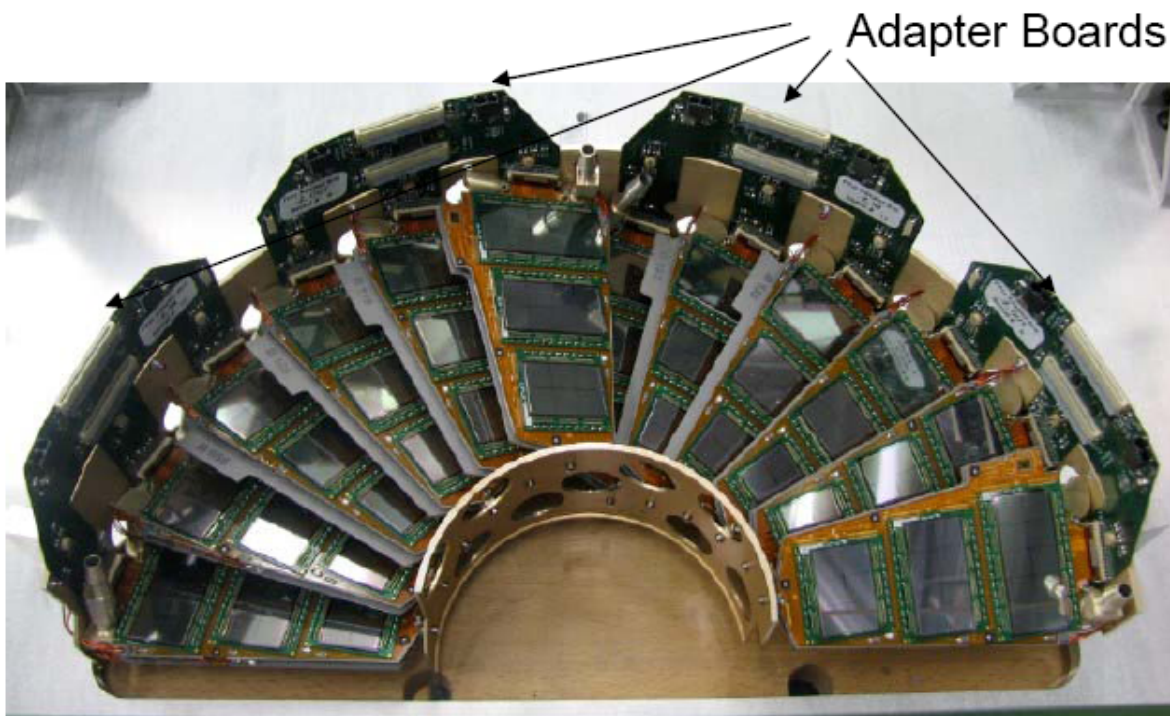


Figure 2-7. Fully instrumented and tested half-disk for the Fpix detector.

### **2.3.1 System Readout for the Fpix**

The readout and control system for the pixel detector consists of three independent components (Figure 2-8): the detector front end, the pixel front end controller (FEC) and the pixel front end driver (FED) [7].

The front end part consists of the TBM and the ROCs. The HUB is the communication port for the TBM. The FEC and FED are electronic boards connected to optical fibers. The FEC sends 40MHz clock and fast control signals, such as trigger and reset, and programs to the front end devices. The FED is used to digitize and format the information sent from the front end part, and send it to the CMS-DAQ event builder. The DAQ (Data Acquisition System) are the hardware and software components to perform the general data acquisition of the detector. Timing and Trigger Control (TTC) boards are used to clock the FEC and FED signals at the LHC frequency. The Trigger Throttling System (TTS) avoids the overflow of information into the DAQ system.

Different hardware devices are used to perform the data acquisition for the CMS Fpix detector. A set of eight adapter boards are used per each disk. An adapter board is a flexible electronic circuit that distributes power and readout control for three blades (Figure 2-9).

The adapter boards communicate the panels with the port cards. The port cards perform the conversion of electrical signals to optical signals, control the DELAY25 chips used for clock adjustment, trigger and digital control data, and host the DCU chips that read the information from the RTDs on the Fpix panels and the sole RTD on the port card. The port cards are connected through optical fibers to the FEC and FED boards.

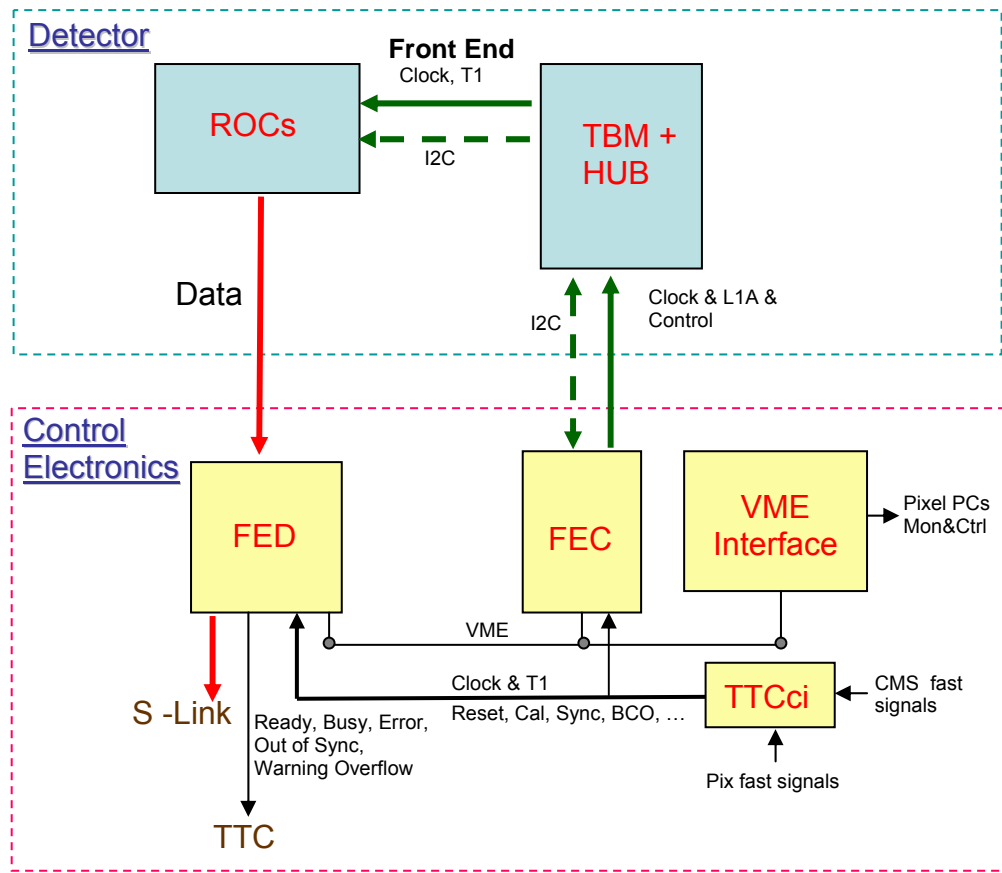


Figure 2-8. Block diagram of pixel control and readout system.

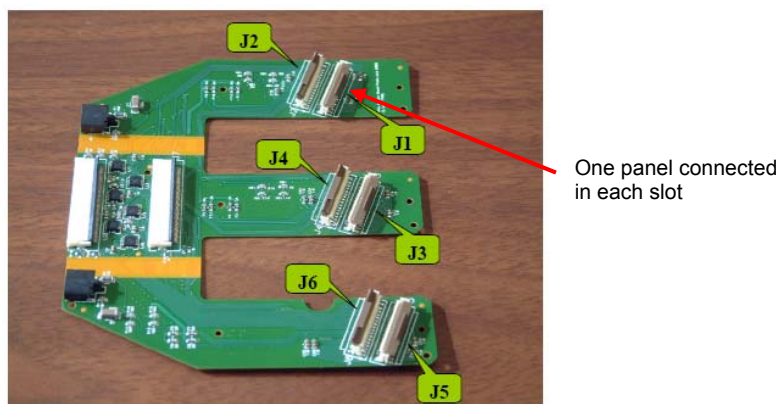


Figure 2-9. Adapter board for the CMS Fpix detector.

## **Chapter 3 – Objectives**

This is a report of four separate projects all related to the CMS forward pixel detector. Each project was designed to contribute to the general tasks of constructing, assembling, and testing of this detector which will form an important part of an experiment whose goals are to study fundamental physics. This chapter and following chapters have been organized accordingly. Specific objectives for each project are presented.

### **3.1. Forward Pixel Beam Test**

- A. Installation of the DCS (Detector Control System) and the SMCS (Slow Motion Control System) for the test of the CMS Fpix detector in the Meson Test facility at Fermilab.
- B. Perform monitoring of temperatures and humidity during the test, to protect the detectors against overheating, overcurrents and humid air condensation.
- C. Monitor data acquisition during the test.

### **3.2. C.A.E.N. SY2527 Power Supply and MSC Cable**

#### **Low Voltage Test**

- A. Measure the basic characteristics of the low voltage channels.
- B. Build a dynamic circuit to simulate the change in load that the CMS Fpix detector will have after an interaction with a particle.
- C. Measure the recovery times for the power supply after a change in load.
- D. Perform tests adding external capacitors to the dynamic circuit to study the effect on the recovery time of the power supply.
- E. Measure the resistance and capacitance of the MSC prototype cable.

## **High Voltage Test**

- A. Perform a high voltage test using a plaquette and the C.A.E.N power supply.
- B. Perform a high voltage test with a different power supply and compare it with the results using C.A.E.N.
- C. Perform a test using the high voltage and low voltage channels simultaneously.

### **3.3. Test Stand for the Partial Forward Pixel Detector**

- A. Assemble the half-disk test stand for the pilot run detector.
- B. Assemble the cold box test stand for the half-service-cylinder.
- C. Perform cooling and humidity tests for the half-disk and half-service-cylinder test stands.

### **3.4. DCS to FEC interface Software**

- A. Develop a software interface to perform the data averaging, transformation and communication of temperatures from the FEC system to the DCS system. This application will be used during the actual CMS run.
- B. Develop a test application to check the interface performance.

## **Chapter 4 - Materials and Methods**

### **4.1 Forward Pixel Beam Test**

Building a detector in particle physics is a complex and long task. After the hardware and software design, assembly and testing of the detector prototype, comes the final production of the real detector. The test of the detector prototype should reproduce the conditions during its use as much as possible. In the case of the Fpix this means providing the right voltages, currents, temperatures and humidity. Control, monitoring and data acquisition systems must be carefully designed. The installation of the Detector Control System (DCS) for the test of the Fpix detector was of vital importance to monitoring environment variables and to protect the detector.

Another important project was the installation of the Slow Motion Control System (SMCS) that allows remote control of small displacements of the Fpix detector with three degrees of freedom. Since the operating temperature of the detector is  $-20^{\circ}\text{C}$ , this important improvement to the test facility eliminated the possibility of misaligning it while opening the temperature-controlled box in order to change its position.

#### **4.1.1 Test beam Facility**

The Meson Test facility (better known as the Test Beam) at Fermilab is the place where we performed a mini fixed-target experiment for the CMS Fpix detector. The Detector Under Test (DUT) was exposed to a pion beam of  $\sim 60\text{Gev}$  as is shown in Figure 4-1.

Two different plaquettes were tested. Before being tested one of the DUT had been exposed to a high radiation dose. The other had not been irradiated. The objective of the test was to determine the change in the detector efficiency due to radiation damage.



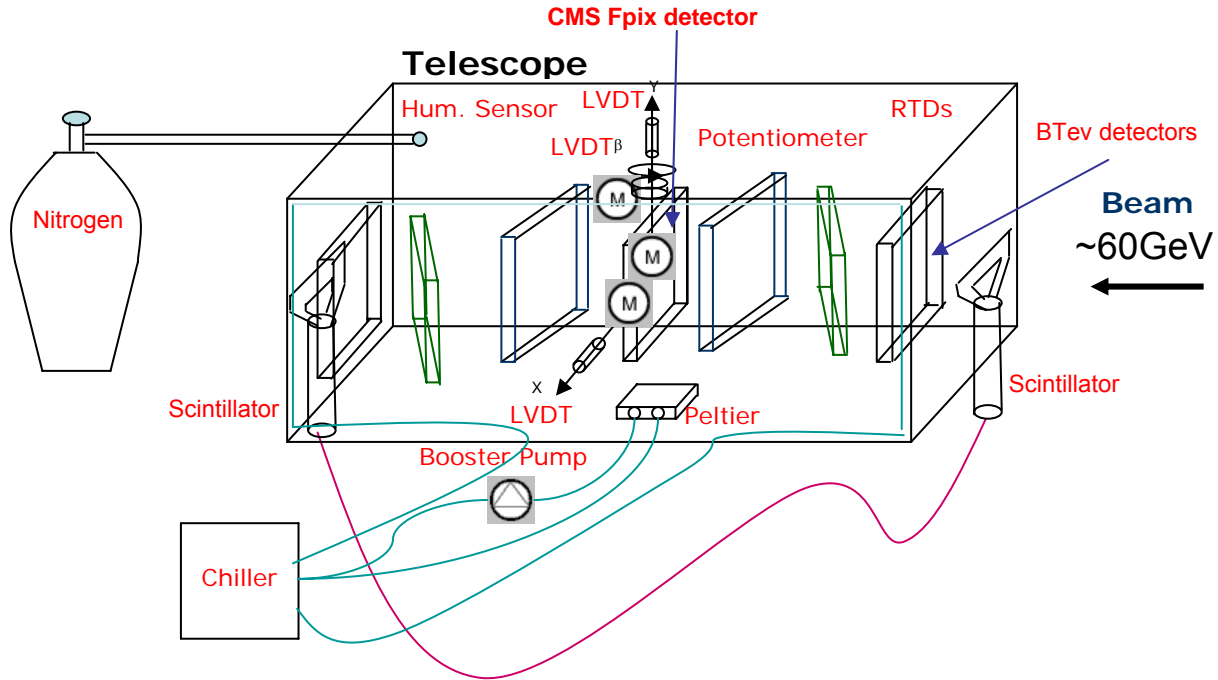


Figure 4-1. Telescope used to test the CMS pixel detector, located at the test beam facility.

The DUT was located in the middle of six other pixel detectors. These detectors (called BTeV detectors) were designed for another experiment and were used to determine the precise location of the pion incident on the DUT on an event by event basis. Such an arrangement is called a “telescope”. The scintillators shown in Figure 4-1 are used as the trigger for data collection. The trigger required that the pion pass through both scintillators.

The cooling system was composed of two different devices. The first part of the cooling system consists of Peltier cells. Jean-Charles Peltier (1785 - 1845), a French physicist, discovered that if a DC voltage difference is applied to a junction of two dissimilar metals, we will find a temperature difference between them [8]. Basically, one side of the junction is going to warm up and the other to cool down.

The second cooling system is the Chiller. This cooling system was used to remove the heat from the Peltier cells as is shown in Figure 4-1 and also to cool down the entire telescope.

The Chiller works by pumping a mixture of water-glycol through cooling tubes that are in contact with the surface of the Peltier cells and the internal edges of the telescope. Peltier cells avoid getting the detector wet if a Chiller cooling line has a leak and allow reaching low temperatures ( $-20^{\circ}\text{C}$ ) faster than with the Chiller alone.

The chiller could by itself reach temperatures down to  $-20^{\circ}\text{C}$  but in a relatively long time. Since the viscosity of the water-glycol mixture increases with decreasing temperatures, it was necessary to use a booster pump to keep a constant flux through the cooling lines.

Dry air (nitrogen) was circulating to keep the dew point below the telescope's temperature. The dew point is the temperature where humidity in air condenses. The nitrogen keeps a low humidity avoiding condensed water from ruining the electronics inside the telescope.

Resistance Temperature Detectors (RTDs) were used to monitor the temperature inside and outside the telescope. The RTDs were made of platinum that has a resistance of  $100\Omega$  for a temperature of  $0^{\circ}\text{C}$ . The Platinum shows a noticeable change of resistance with a change in temperature. The physics behind this phenomenon is that there is an increase in the number of conduction electrons in the material with increasing temperature. For a constant voltage, this change can be calibrated to obtain the relationship between temperature and current.

#### **4.1.2 DCS and SMCS installation**

The DCS records temperatures, humidity and dew point inside and outside the telescope at the test beam setup protecting the system against overheating and overcurrents.

The Slow Motion Control System (SMCS) has three degrees of freedom: X (horizontal displacement), Y (vertical displacement) and  $\beta$  (azimuthal rotation) as is shown in Figure 4-1. This allows changing the position of the detector remotely with respect to the incident beam to study the detector's performance as a function of incident angle. Both systems are composed of

Siemens modules controlled through a PVSS interface. A schematic diagram of the configuration is shown in Figure 4-2.

The Siemens PS 307 power supply provides the required voltage of 24V for the modules in the three first rails as is shown in Figure 4-2. Each Simostep step motor controller works with an independent power supply that provides a 3-phase voltage of 325V. The CPU 315 PLC controls all the processes executed for the modules using a Siemens software interface installed into an external computer located in the control room. One module IM 360 and two modules IM 361 establish the communication between modules in different rails. The CP 343 performs the Ethernet communication process between the CPU 315 PLC and the computer in the control room. Module SM 323 controls the digital input and digital output signals (DI/DO) used to perform the switch of the Booster pump, the Peltier power supply and the Chiller. The SM 331 AI (Analog Input) is used to receive analog signals from the LVDT's (Linear Variable Differential Transformers) and the humidistat and convert them to digital. A LVDT is an electromechanical transducer that converts rectilinear motion of a mechanical system into an electrical signal (Figure 4-1). The SM 331 RTD receives analog signals from different RTDs and converts them into digital. The SM 332 AO (Analog Output) controls the Peltier elements and the step motors that adjust the position of the Telescope box.

Function Manager Modules FM 353 control the process of stepping and the direction of motion ( $\pm X, \pm Y, \pm \beta$ ) for each degree of freedom. The FM 353 sends analog signals to the Simostep motor controller that converts them into angular movement by appropriate current feeds to the motor windings.

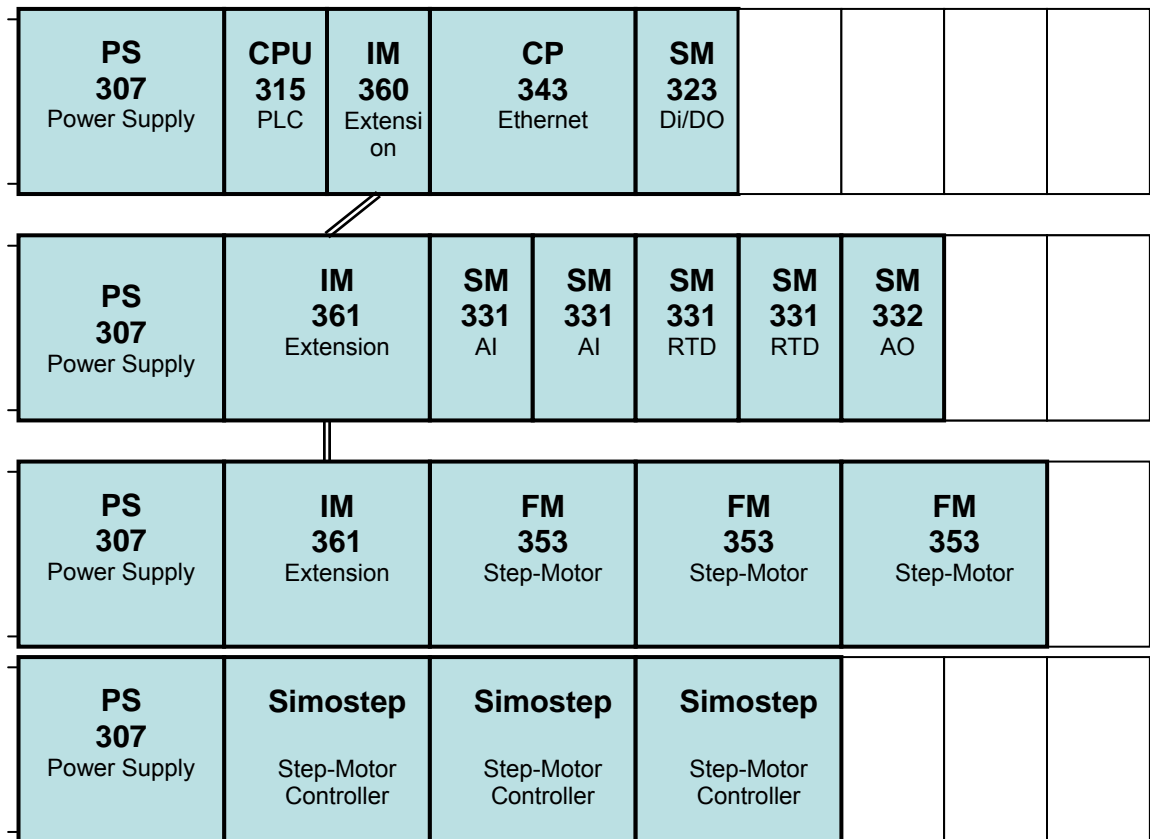


Figure 4-2. Schematic diagram of the Siemens Modules distribution.

Figures 4-3, 4-4 and 4-5 show the installed Siemens modules on the rails at the test beam facility.

DIN means "Deutsche Industrie Norm". It is a German word (Siemens is a German Company) for an engineering standard that describes the piece of metal (width and shape) on which the Terminal Blocks are mounted. In Figure 4-4, DIN 0, DIN1 and DIN 2 label the locations of the rails at the back of the RR05 rack where are located the terminal blocks for: (A) power distribution, (B) fuse boxes and (C) terminal blocks for distribution of digital and analog signals (C).

Figure 4-5 shows the bottom half of the RR05 rack. DIN 3 has terminal blocks for power distribution and DIN 4 has circuit breakers for each step motor. The terminal blocks on DIN 3

are for 24V power distribution and the circuit breakers on DIN 4 are for the 3-phase AC voltage of 325V necessary to power up each step motor. We can see on REAR 0 the power supplies that provide the 24V for the Siemens modules and on Rear 1 the power supplies for the step motors.

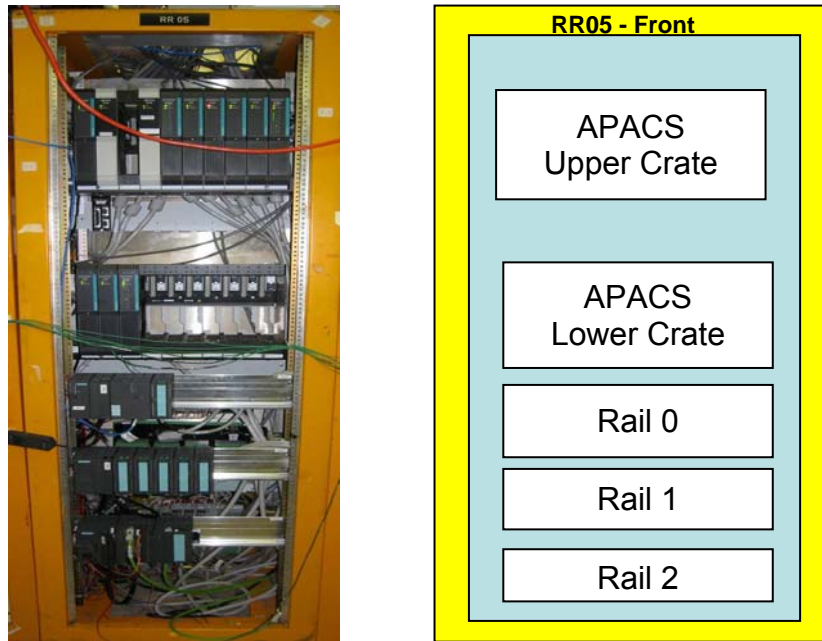


Figure 4-3. Front view of the DCS rack RR05 for the Fpix detector in the test beam facility. APACS is the monitor and control system replaced by DCS.

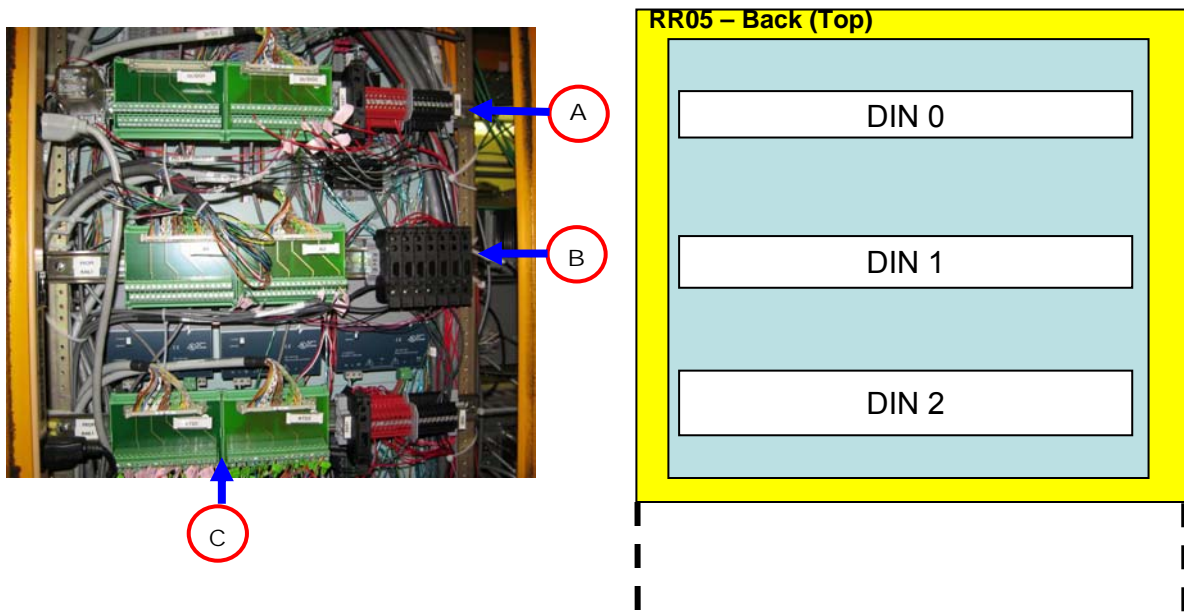


Figure 4-4. Back view of the top half of the DCS rack RR05 for the Fpix detector in the test beam facility. A) Terminal Blocks for power distribution of 24V, B) Fuse boxes to protect the system against overcurrents, C) terminals which distribute analog and digital signals.

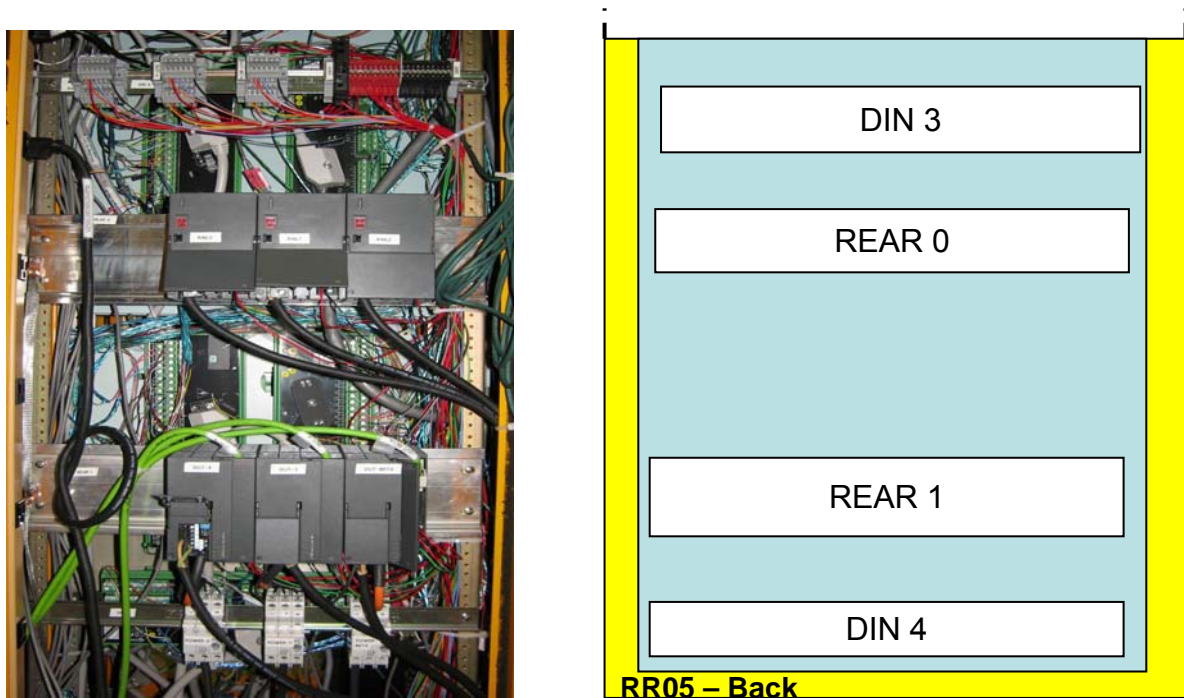


Figure 4-5. Back view of the bottom half of the DCS rack RR05 for the Fpix detector in the test beam facility.

### 4.1.3 Power distribution diagram

Electrical safety regulations at Fermilab required the preparation of a power distribution diagram with all the electrical connections on it. An official inspection by the Electrical Safety Department of Fermilab was necessary to receive the authorization to use the DCS and SMCS systems at the test beam. Voltages, currents, type of fuses, and wire gauges are items that have to be specified on the diagram. Figures 4-6, 4-7 and 4-8 show the power distribution diagram prepared as part of this thesis project and presented to Fermilab. The legend on the diagrams indicates the American Wire Gauge (AWG), the number of individual strands per wire, and the maximum driving current rating for the wire.

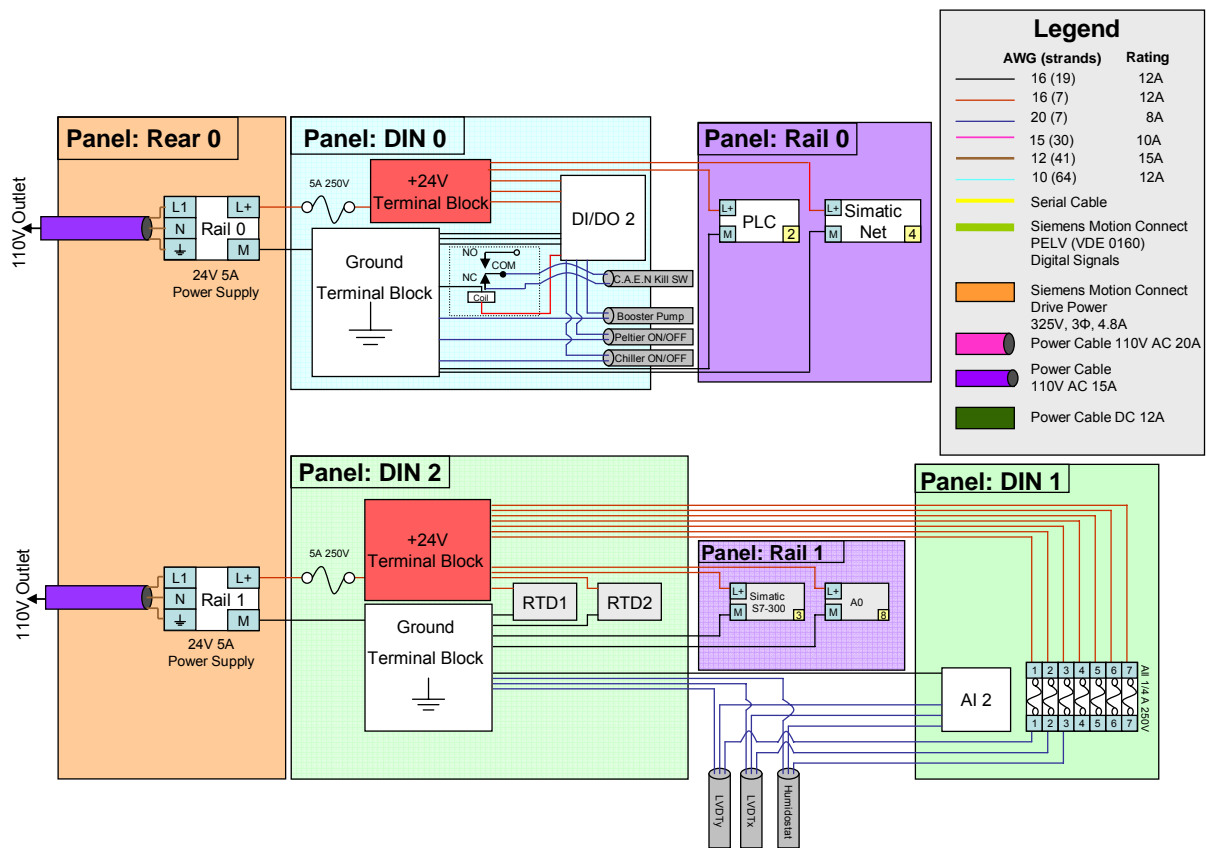


Figure 4-6. Power routing diagram one for the DCS and SMCS systems at the test beam facility.

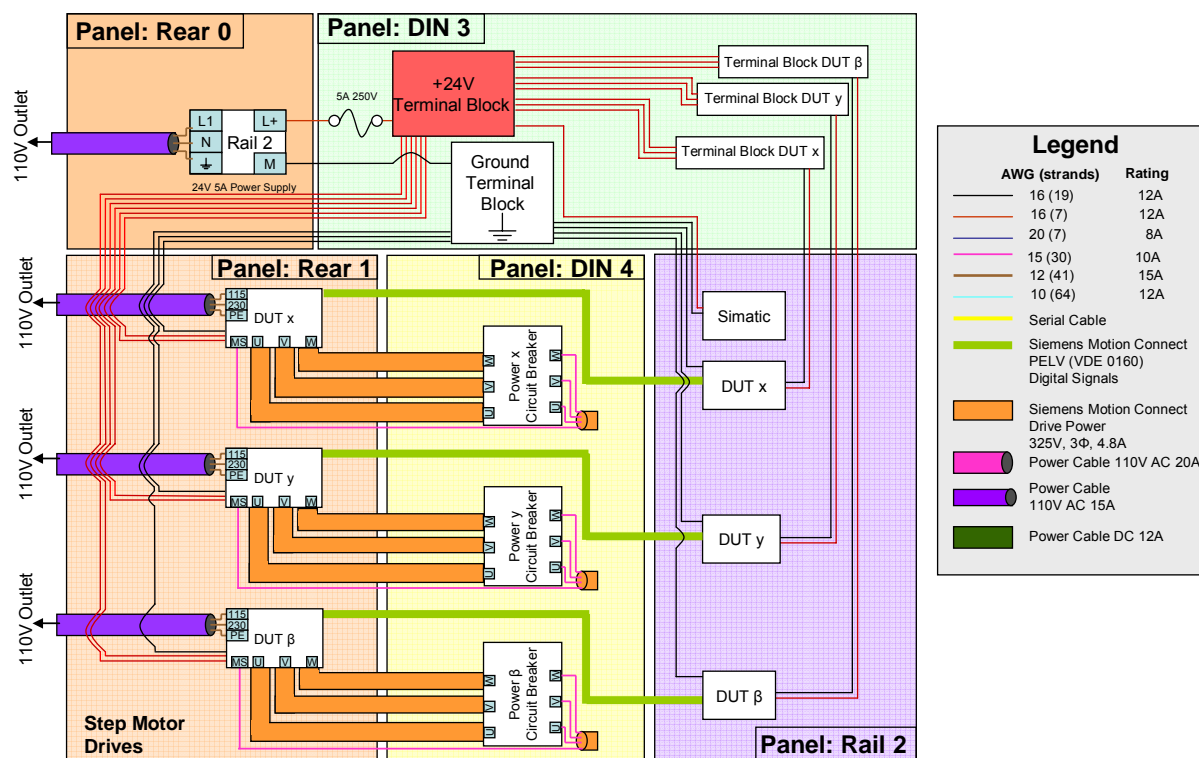


Figure 4-7. Power routing diagram two for the DCS and SMCS systems at the test beam facility.

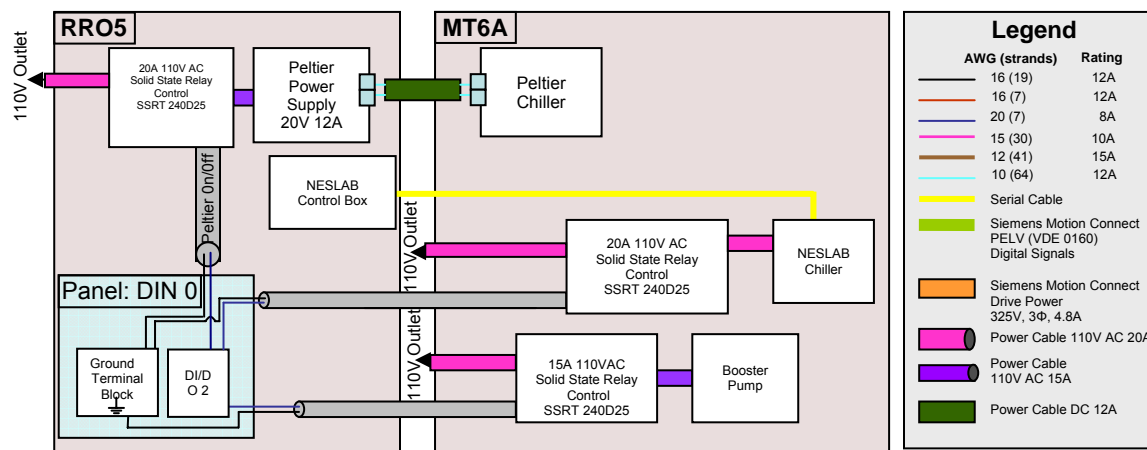


Figure 4-8. Power routing diagram three for the DCS and SMCS systems at the test beam facility.



#### **4.1.3.1 Data acquisition**

The data acquisition of the beam test of the Fpixel detector was performed according with the following methodology. The first step was to check the nitrogen level in the cylinder and to open the nitrogen flow meters. After this process we recorded the initial temperatures on the detectors and testing area. Once the dew point was under  $-10^{\circ}\text{C}$  we setup the chiller and the Peltier to the required value of temperature for the run. When the detector reached the run temperature, we called to the beam main control run at Fermilab where is performed the control of the accelerator and asked for the beam at the energy required for the run. After checking the beam intensity and initializing the software to record the data, we monitored constantly the number of coincidences between the events on the Fpix detector and the events on the BTeV detectors.

An important parameter of study during the test was the variation of the voltage threshold. The voltage threshold is used to discriminate signals. If a signal is below the threshold value, it is not registered as a possible event and is not stored. Signals above the threshold value are considered as candidates to be events. The threshold is used as a filter that allows us to eliminate noise.

Another important topic studied during the beam test was the bias voltage. Applying different bias voltages we studied the detectors performance. Since the detector will be exposed to a high radiation dose in CMS, the sensor will suffer progressive degradation due to the damage to the semiconductor material which will increase the number of recombination sites. This will make necessary an increment of the bias voltage applied to the sensors to avoid efficiency loss as much as is possible.

## **4.2 C.A.E.N. SY2527 Power Supply and MSC Cable**

The C.A.E.N. SY2527 power supply is the system that will be used to provide the power for the Forward pixel detector of CMS. The MSC cable characteristics, the recovery time of the power supply after an interaction, and the low and high voltage performance of this system are factors that need careful study.

### **4.2.1 C.A.E.N. components**

The CMS Fpix detector will use the C.A.E.N. power supply for the readout system, the control electronics of the detector and to bias the sensors. The C.A.E.N. power supply has two main components; the first one is the controller C.A.E.N. SY2527 mainframe that has three sections (See Figure 4-9), the *board section* with six slots to house boards, distributors and branch controllers, the *power supply section* and the *CPU and front panel section* which includes all interface facilities [9]. The second component of the power supply is the LV/HV module A4603 that has two channels PSU0 and PSU1. Programmable parameters for each power channel include two values of voltage: V0set and V1set, and two current limits: I0set and I1set. Each channel can be programmed with a maximum value of voltage and current. The board has a hardware protection for ISET values of current that are higher than the power supply tolerance. The IMon value shows the magnitude of current on the monitor that for higher values than the programmed maximum value (Imax) triggers an overcurrent alarm.

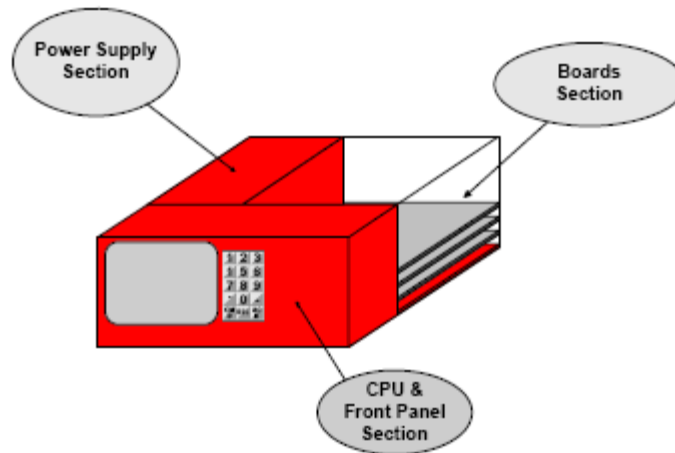


Figure 4-9. Layout of the main mechanical section of the SY2527 mainframe.

#### 4.2.2 CDF and MSC cables

Since the prototype cable for the detector was not available when we began testing, the first test for the power supply was done with a replacement cable which we will call the CDF (30m long). The cross section of this cable is shown in Figure 4-10. These preliminary tests allowed us to develop the testing procedure.

The prototype MSC cable is 40m long. According to the cable specifications it has two pairs of twisted wires each of  $9.0\Omega$ , ten single wires of  $14.6\Omega$  and six single wires of  $0.2\Omega$ . The cross section of the MSC cable is shown in Figure 4-11 and the description of the wire material and the dimensions of each one are in Table 4-1.

Two values of low voltage of 2.5V and 1.75V were used in the test. These are the low voltage values that will be used to power the digital and analog part of the ROCs (readout chips).

Four wires of  $0.2\Omega$  were implemented for a connection of 2.5V; the other two wires were used for a connection of 1.75V. For each low voltage, we used one pair of the twisted wires as sense wires.

The high voltage test was simply a measurement of leakage current versus bias voltage (provided by the power supply) applied to a forward pixel plaquette. The high voltage connection was made with two wires of  $14.6\Omega$  resistance.

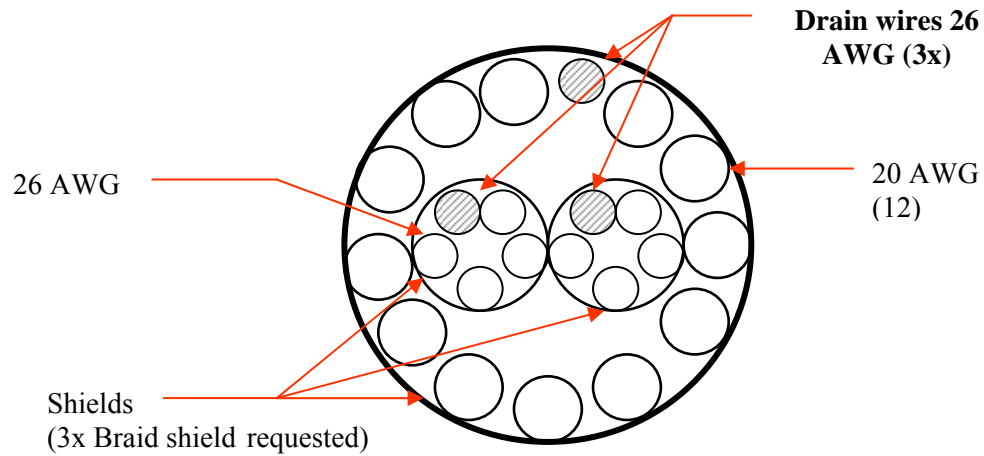


Figure 4-10. Cross section of the CDF cable.

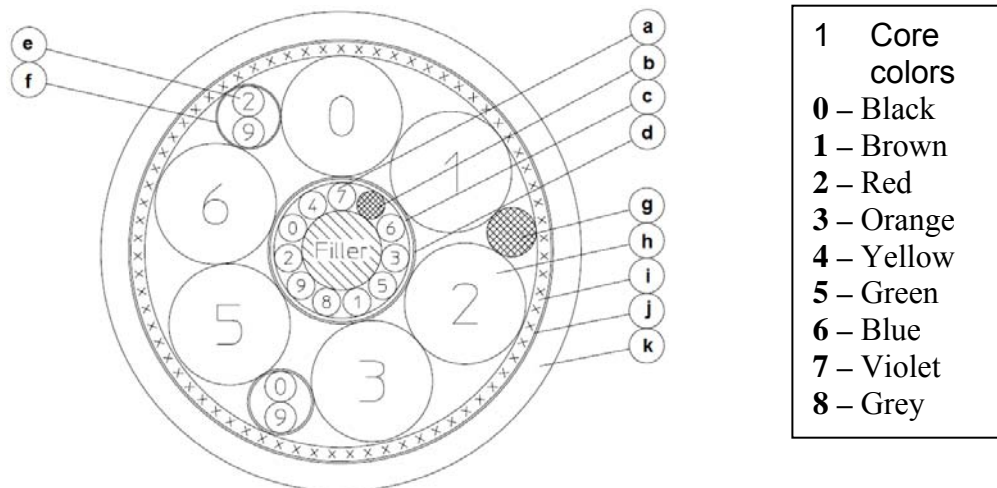


Figure 4-11. Cross section of the MSC cable.

Table 4-1 – Description of the MSC cable.

All linear dimensions in mm.

Position	Description	Dimensions	Overall diam	Strands (diam)
<b>a</b>	Tin-plated copper conductor insulated with PE (polyethylene)	AWG 30	0.30/0.70	7(0.10)
<b>b</b>	Drain wire of tin-plated copper	AWG 24	0.6	19(0.127)
<b>c</b>	Aluminum/polyester film		3.6	
<b>d</b>	Polyester film		3.7	
<b>e</b>	Tinplated copper conductor insulated with PE	AWG 28	0.38/0.78	7(0.127)
<b>f</b>	Polyester film (optional)		1.66	
<b>g</b>	Drain wire of tinplated copper	AWG 18	1.2	19(0.254)
<b>h</b>	Tinplated copper conductor insulated with PE	$A = 4\text{mm}^2$	2.48/3.28	56(0.30)
<b>i</b>	Braid of tinplated copper wire	Wire diam 0.16	11	mon cov 85%
<b>j</b>	Polyester film		11.1	
<b>k</b>	Jacket of PE	T=0.7	12.5	

### 4.2.3 Low voltage test setup

The setup for the low voltage test was made with the detector characteristics in mind. The detector will work with low voltages of 2.5V and 1.75V required to power the digital and analog part of the readout chips. Figure 4-12 shows the circuit diagram for the low voltage test. The test setup was built with eight load resistors of 0.1, 1.2 and 1.6 ohms connected in parallel and that group connected in series to a jumper used to change the load. The sense wire was used to monitor and control the voltage at the circuit. A square wave generator was connected in parallel to the load resistance through the FET section. This acted as an electronic switch for the current. The fast switching of current was an external perturbation of the circuit that simulated the change of current that we will have in our pixel during the experiment. The signals were recorded with a digital oscilloscope.

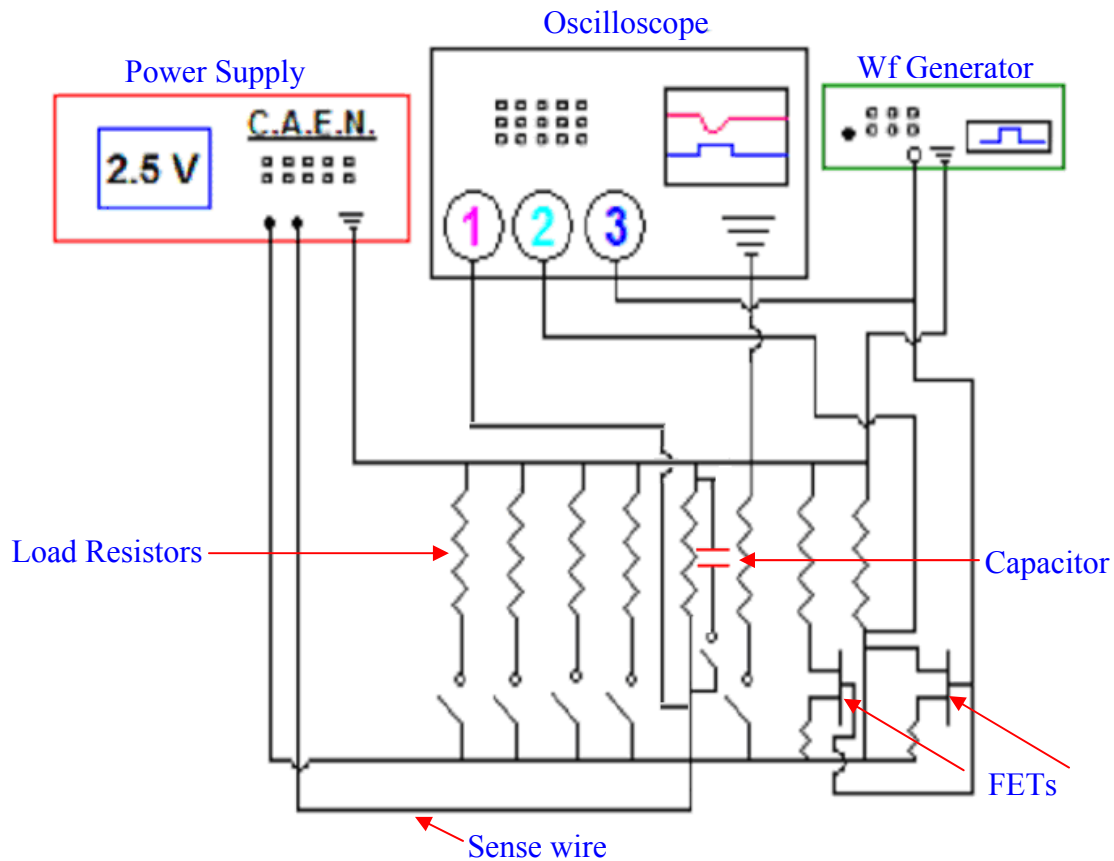


Figure 4-12. Diagram of connections for the cable high voltage test.

### 4.3 Test Stand for the Forward Pixel Detector

SiDet, the Fermilab silicon detector facility, is the location where panels and plaquettes are tested and where the half-disks for the CMS Fpix detector are assembled. Prior to shipment to CERN, a test of the assembled detector (as will be installed at CERN) is necessary in order to detect any problems which may have occurred in the final assembly step. The first detector (for the engineering run) will consist of two half-disks each one with only two blades instrumented but the length of the service cylinder (in this case half a cylinder) is the same as in the full detector (Figure 4-13). The service cylinder is the space where the power, cooling and data lines for the detector run.

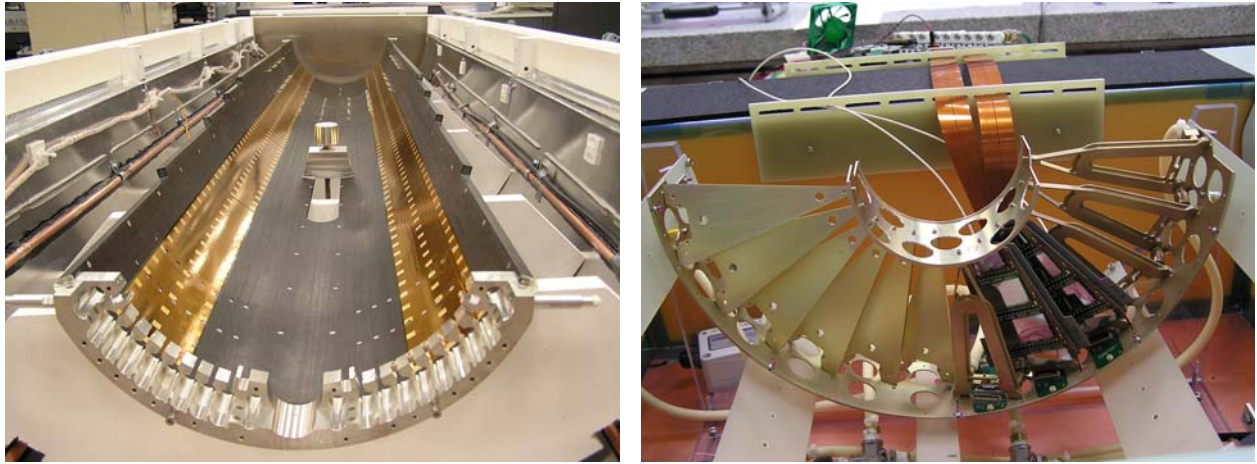


Figure 4-13. Assembly of the partial forward pixel detector. The service half-cylinder (left). The half-disk with two blades instrumented.

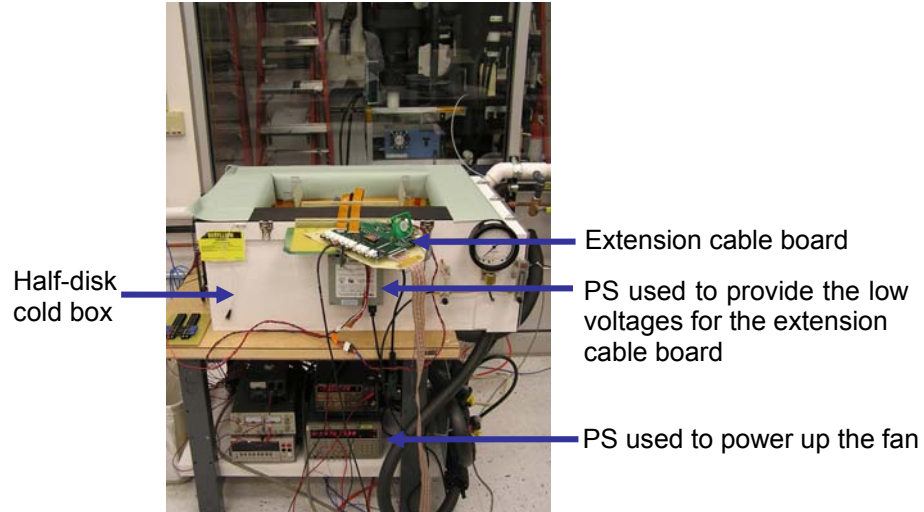
### 4.3.1 Half-disk cold box

In order to provide the run environment, the University of Northwestern built a cold-box which is a controlled space to house the detector while it is being tested. In collaboration with the University of Colorado we assembled the half-disk test stand. We installed the instrumentation for the cold box: RTDs (Resistance Temperature Detector), humidity sensors and pressure sensors. All external components like the cooling system, the power supplies and computers for the readout system were also implemented.

Three power supplies (PS) were used to power up the detector. One PS provides the high voltage necessary to bias the sensors, a second one supplies the required low voltages for the extension cable board (ECB) and a third one powers up the fan on ECB (Figure 4-14. a and b).

The ECB works as the port card for testing purposes of the half-disk at SiDet. This board sends and receives analog and digital signals from and to the panels on the half-disk through the adapter board.

(a)



(b)

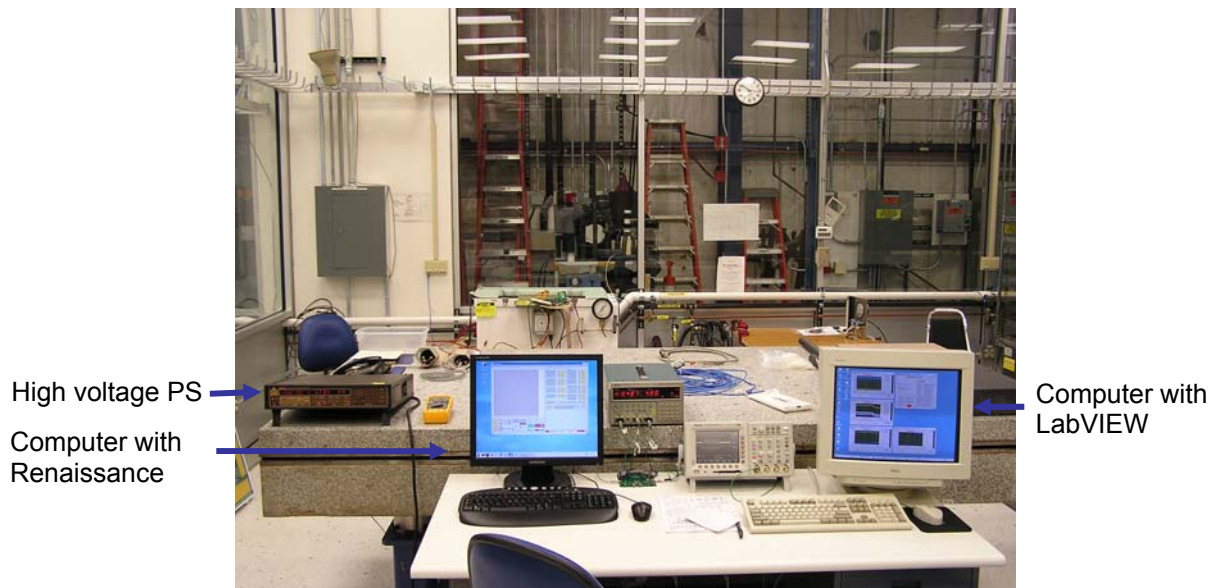


Figure 4-14. (a) Half-disk cold box and power supplies for the extension cable board. (b) High voltage power supply and test stand with computers to test and monitor the half-disk for the Fpix detector.

The ECB board has voltage regulators to provide the exact voltage for the ROCs. These voltage regulators convert the 5V originally provided from the PS to 2.5V and 1.5V required for



the digital and analog components of the electronics respectively. Figure 4-15 shows a more detailed image of the Extension Cable Board.

Renaissance is special software to perform plaquette and panel testing [10]. The test consists of a study of the address level separation, a pixel by pixel threshold trimming, detection of faulty pixels and bump bonds, and detailed measurements of the gain curve and threshold curve for each pixel [11]. Temperatures, humidity and differential pressure of the fluid into the cooling lines are monitored with LabVIEW™ software.

We installed the cooling system (Figures 4-16 and 4-17) and the dry air (nitrogen) to the box. Fluorocarbon was used to cool down the detector. In case of a leak into the cooling lines, the fluorocarbon evaporates rapidly avoiding getting the detector wet and causing damage to the electronics. We performed a cooling test reaching temperatures down to -10 °C.

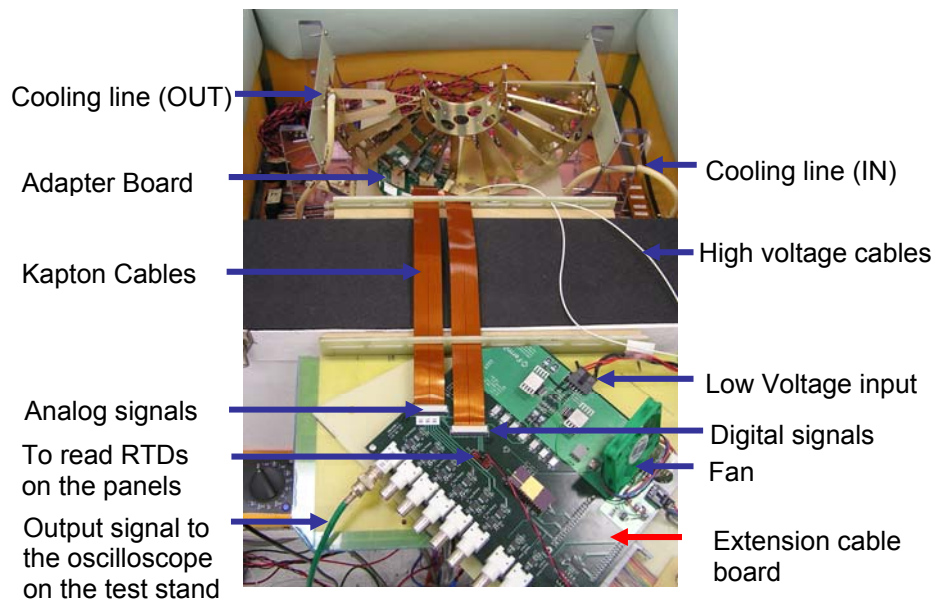


Figure 4-15. Extension Cable Board to test the half-disk for the CMS Fpix detector.



Figure 4-16. Chiller for the half-disk test of the CMS Fpix detector.

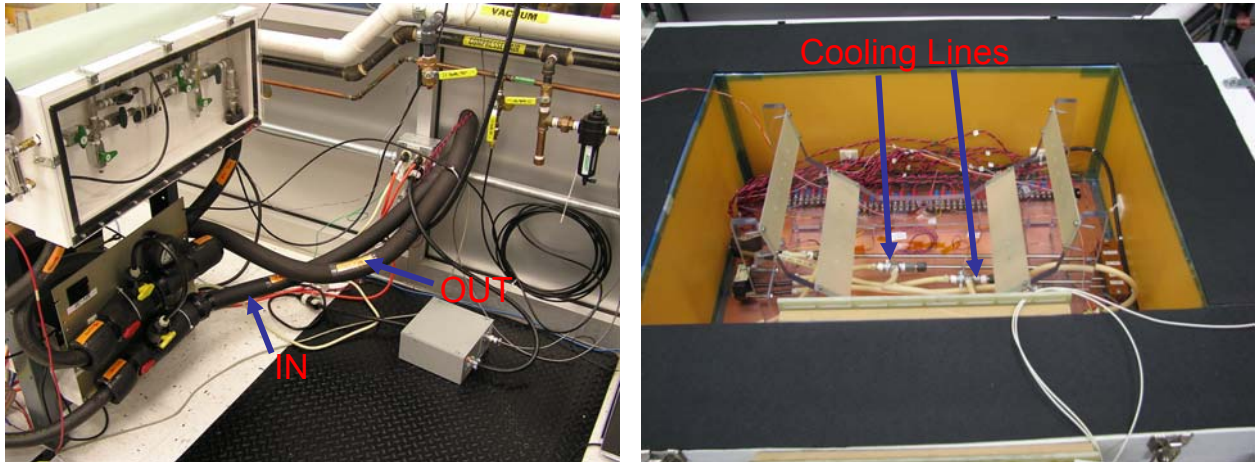


Figure 4-17. Routing for the cooling lines of the half-disk test cold box for the CMS Fpix detector. (Left) Cooling lines outside the half-disk cool box connecting with the Chiller shown in figure23. (Right) Cooling lines inside the half-disk cold box (see figure22).

#### 4.3.2 Shunt Resistor for analog current measurement from the ROCs

A shunt resistor consisting of ten resistors connected in parallel each one of  $1\Omega$  was built to measure the analog current required for the ROCs. By measuring the voltage drop on the  $0.1\Omega$  shunt resistor with a high precision voltmeter (Figure 4-18), we were able to measure the current in the power line. In order to work properly, the ROCs have to be provided with an analog current of 24mA.

The procedure to setup the correct  $V_{ana}$  for the ROC's has three steps:

1. Set  $V_{ana}$  register of a certain ROC under test to 0 (no analog current absorbed by the ROC).
2. Record the current absorbed by the panel (i.e.  $I_0$ ).
3. Adjust the  $V_{ana}$  register such that the actual current (i.e.  $I_1$ ) minus  $I_0$  is  $\sim 24\text{mA}$   
( $I_1 - I_0 = 24\text{mA}$ )

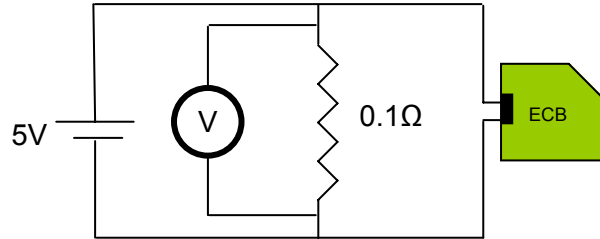


Figure 4-18. Circuit diagram for the shunt resistor connection.

### 4.3.3 Half-Service-Cylinder Cold Box

The University of Colorado built a cold box prototype for the half-service-cylinder, to perform a complete test of the detector and its components (i.e. port cards, external cooling lines). The box was fully instrumented with RTDs, humidity sensors, cooling system (Chiller: water-glycol), C.A.E.N power supply, DAQ with FEC and FED boards (Figure 4-19) and a computer set up for the PVSS system.

## 4.4 DCS to FEC interface Software

As explained in section 2.3.1 the FEC and FED are used for data acquisition and control signals of the detector. The data acquisition is classified in two types: events data and conditions data. Conditions data includes temperatures, humidity, voltages and current. The conditions data has to be monitored in order to know and provide the right environment for the detector and protect it against overheating, overcurrents and high humidity.

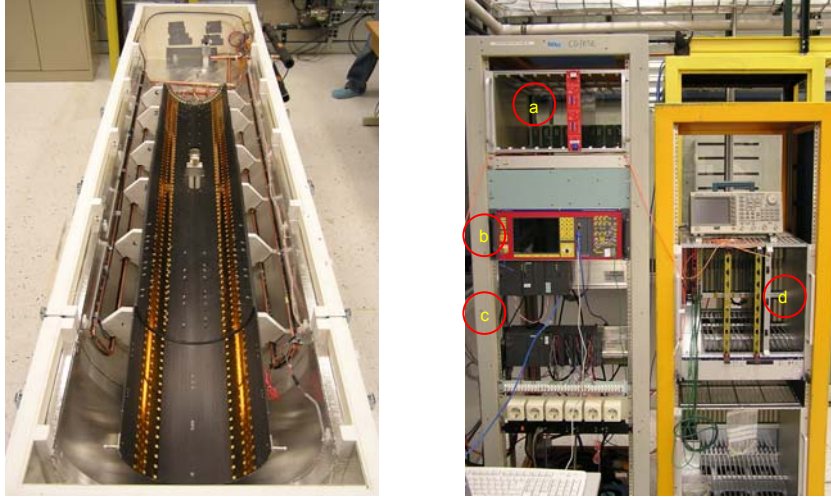


Figure 4-19. Cold box and electronic devices for the Half-service-cylinder at Sidet. (Left) Half-service-cylinder inside the cold box. (Right) electronic devices, a) CAEN 4603 power supply board, b) CAEN SY2527 control module, c) DCS system, d) FEC and FED boards.

A programming language called PVSS will be used for graphical monitoring of the conditions data. The conditions data will be stored in a database called Conditions database. In order to read the information from the FEC and FED and send it to the PVSS, a software program was developed using the XDAQ framework. XDAQ is based on the C++ programming language and provides libraries and classes for software development. The basic idea of using XDAQ is to provide a uniform way of programming and a variety of software tools that simplify the programming process. Figure 4-20 shows the software design implemented to read, send, control and store the information from the FEC board into the Conditions database. The communications process between the XDAQ applications and the PVSS interface is made through the PSX server. The PSX server is a XDAQ implementation to communicate with applications that do not use the XDAQ framework, such as PVSS.

The PixelSupervisor is a XDAQ application developed by the Cornell University group. The PixelSupervisor controls the initialization process, the Finite State Machine (FSM), and the readout data for each card (FEC and FED) through two XDAQ applications called

PixelFECSupervisor and PixelFEDSupervisor. The FSM state summarizes the current status of an application.

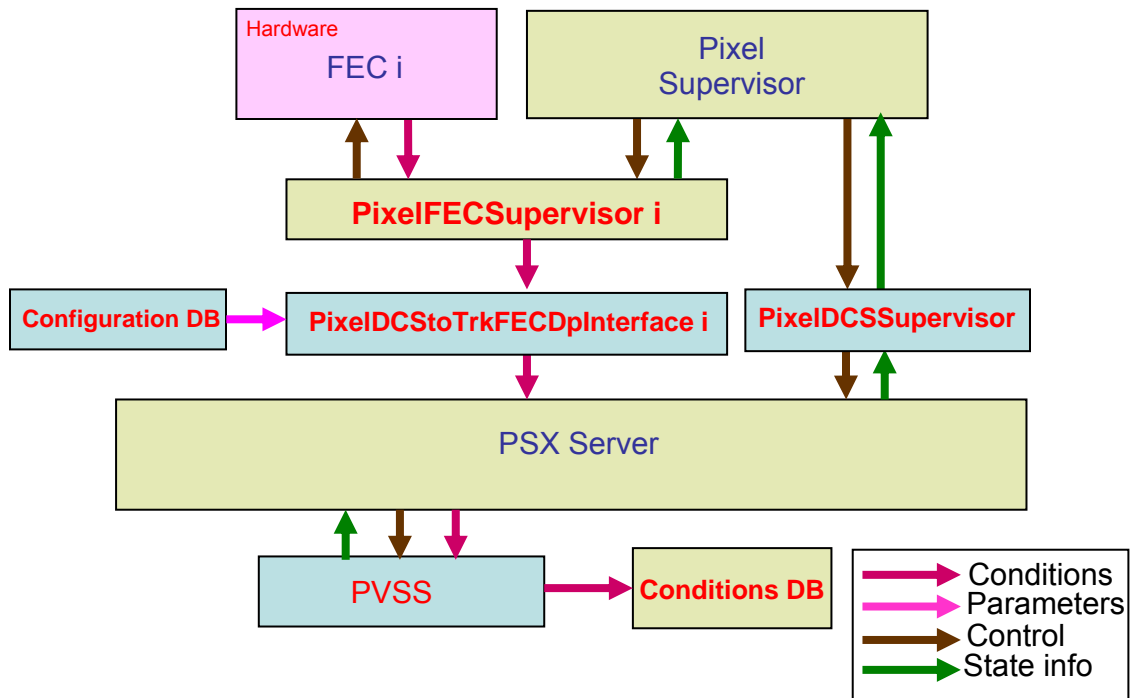


Figure 4-20. Flow of information and control in the pixel data acquisition system.

The PixelFECSupervisor performs the configuration and control of the acquisition of conditions data from the FEC boards. The PixelDCSSupervisor is the XDAQ application that will control and monitor the Detector Control System (DCS) via the PSX server. This application was developed by a group of the University of California at Davis.

Our task was the development of the PixelDCStoTrkFECDpInterface, a XDAQ application to send temperatures and voltages via the PSX server to the DCS. The interface was written in C++. A set of calibration constants (parameters) and names of PVSS data points have to be extracted from the Configuration database in order to transform and send the information to PVSS. This will be explained in more detail in section 5.4. The PixelDCStoTrkFECDpInterface application gets its input from the PixelFECSupervisor. Each second, the PixelFECSupervisor

will read information of temperature from thousands of sensors on the Fpix detector (one per ROC) and send it to the PixelDCStoTrkFECDpInterface using SOAP [12] (Simple Object Access Protocol) messaging. A SOAP message is a standard protocol to exchange data among computers. Once the information is received by the PixelDCStoTrkFECDpInterface, it is processed and either sent or not (a dead band condition is applied) to the PVSS software through the PSX server.

#### 4.4.1 SOAP Message Format

A SOAP message is constructed from a set of nested XML tags that contains information in a well organized way. The basic structure of a SOAP message is:

```
<SOAP-ENV: Envelope
  xmlns : SOAP-ENV=http://schemas.xmlsoap.org/soap/envelope/
  SOAP-ENV: encodingStyle=http://schemas.xmlsoap.org/soap/envelope//>
  <SOAP-ENV: Body>
    <xdaq::myMessage1 xmlns::xdaq="urn:xdaq-soap:3.0"/>
    <xdaq::myMessage2 xmlns::xdaq="urn:xdaq-soap:3.0"/>
    .
    .
    .
  </SOAP-ENV: Body >
</SOAP-ENV: Envelope>
```

The “Envelope” tag is used to wrap the body of the message and gives access to the SOAP elements within the message. The Body contains a set of lines each one of which is called a “child element”. The child elements can have attribute elements to provide additional information in the message [13] as we will see in section 5.4.

#### 4.4.2 Tasks of the PixelDCStoTrkFECDpInterface

The tasks for the PixelDCStoTrkFECDpInterface are:

1. Access the Configuration database and retrieve tables containing transformation constants and the names of the PVSS data points.

2. Decode SOAP messages sent by the PixelFECSupervisor.
3. Convert the raw ADC values recorded by the FEC boards to physical units (Temperatures, Voltages).
4. Calculate a “running average” for each channel. The formula for the running average is:

$$Ave_{i+1} = 0.99 * Ave_i + DpValue_{i+1}/100 \quad (1)$$

By means of this formula, the statistical weight of the first values decrease exponentially and the last measurement has the highest significance. Averaging is needed to eliminate fluctuations. The formula used reacts more quickly to changes in the conditions than a normal average.

5. Apply a dead band condition; only send those data points to PVSS whose value has changed by more than a certain amount. This ignores fluctuations.
6. Compose and send a SOAP Message to PVSS through the PSX Server. For performance reasons all the data points that pass the dead band condition are sent in a single SOAP message.

#### **4.4.3 Running XDAQ**

XDAQ applications can be loaded into the XDAQ executable at run time. The XDAQ executable is a web interface accessible through an ordinary web browser. Figure 4-21 shows the browser display for the PixelDCStoTrkFECDpInterface.

To test the PixelDCStoTrkFECDpInterface application a XDAQ test application called PixelDCSMessage was developed. This test application sends to the PixelDCStoTrkFECDpInterface a SOAP message of the same format that the PixelFECSupervisor will send in the actual running.

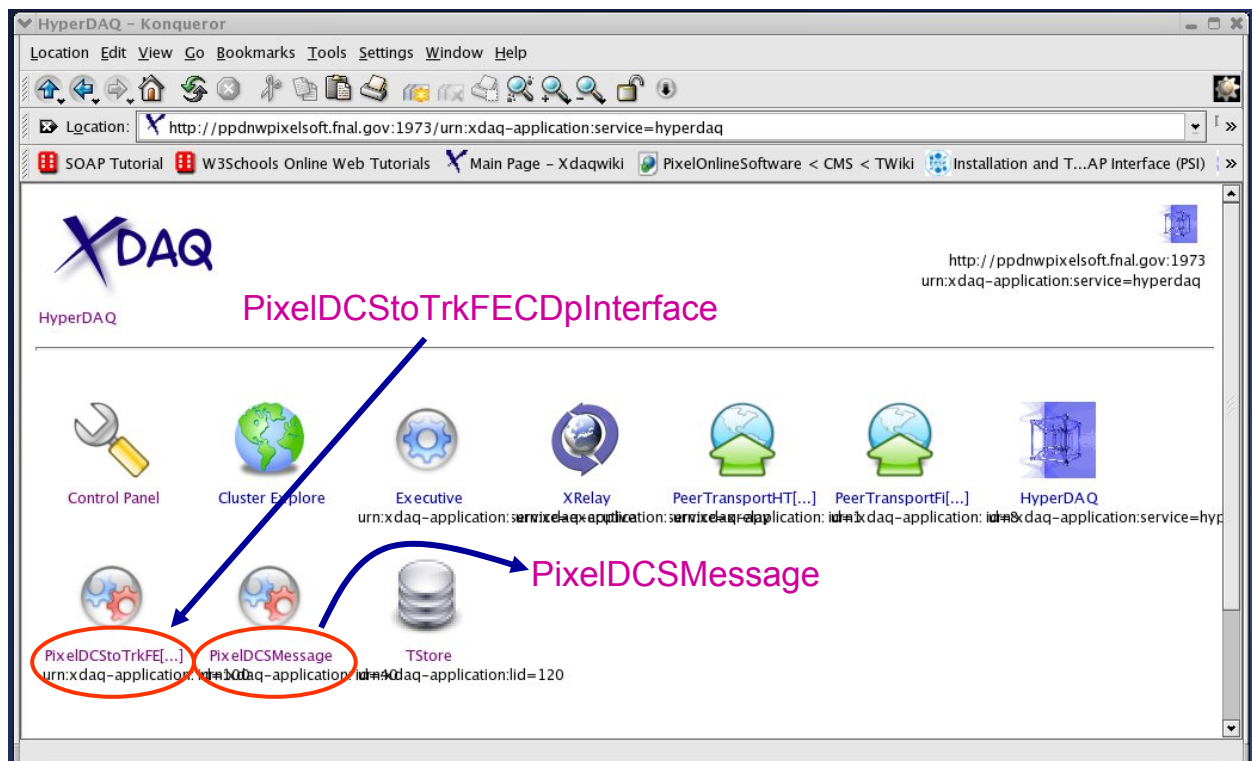


Figure 4-21. XDAQ browser display which includes the PixelDCStoTrkFECDpInterface application.



## **Chapter 5 - Results**

### **5.1 Forward Pixel Beam Test**

#### **5.1.1 DCS Results**

The DCS monitored and controlled the environmental parameters for the beam test performed during the summer of 2006. Tables 5-1 and 5-2 summarize the information of temperatures during this period. The measurement of the nitrogen level was another important task. Table 5-3 presents the daily measurements of it. Two flow meters (fine and regular adjustment) were used to regulate the nitrogen circulation inside the telescope. Figure 5-1 shows a graph of Nitrogen Level vs. Time used to estimate the day that a new nitrogen cylinder had to be ordered.

#### **5.1.2 Test beam results**

We participated actively in the data taking of beam tests in January-February and July-August of 2006. The results of the first beam test have already been analyzed by physicists from the INFN Institute of Milan, Italy. The results indicate that the irradiated plaquettes work well and do not have a significant damage. Figure 5-2 shows the results of the efficiency of an irradiated plaquette. The efficiency is almost 100%. The efficiency was calculated in terms of the number of coincidences between the events on the Fpix detector and the BTeV detectors, divided by the number of events in the BTeV detectors. Other aspects such as the number of bad bump bonds and the bias voltage applied to the detector were taken into consideration to perform the analysis.

Table 5-1 - Temperature data for the beam test in July, 2006. DP (Dew Point), DUT (Detector Under Test), CP (Cold Plate: aluminum plate where are located the Peltier Cells that cool down the detector), Chiller S (Chiller Supply: temperature of the coolant at the entry point), Chiller R: (Chiller Return: temperature of the coolant at the exit point), Box air is the air temperature inside the telescope. Y11, X10, X5, X4 and Y3 correspond with the temperatures of the BTeV detectors. Due to technical problems we were not able to monitor the temperature of 1 BTeV detector (X9).

Temp (C)						
Time	7/12 - 16:30	7/13 - 09:26	7/13 - 15:57	7/13 - 20:00	7/14 -	7/14 - 15:00
DP	-14.20	-17.30	-16.86	-16.81	-17.23	-17.21
DUT	20.97	19.65	19.84	20.04	20.38	20.21
CP	19.48	18.26	18.45	18.65	18.62	18.75
Chiller S	15.08	14.20	14.15	14.30	14.35	14.54
Chiller R	18.89	17.72	17.92	18.14	18.16	18.33
Box Air	22.73	21.36	21.39	21.56	20.97	21.19
Y11	24.49	22.73	23.15	23.39	22.83	22.97
X10	25.82	24.00	24.45	24.74	24.18	24.25
X5	24.99	23.15	23.59	23.86	23.74	23.97
X4	26.02	24.15	24.59	24.86	24.23	24.37
Y3	23.87	21.92	22.39	22.61	21.97	22.19
Temp (C)						
Time	7/15 - 09:00	7/15 - 15:20	7/16 - 09:15	7/16 - 15:20	7/17 - 09:38	7/17 - 15:17
DP	-18.86	-19.18	-17.12	-18.69	-18.54	-0.49
DTU	-10.61	-10.29	14.69	-2.04	-4.16	12.96
CP	-17.57	-17.40	9.40	-10.37	-15.78	5.33
Chiller S	-2.01	-1.99	10.35	-7.33	-4.74	0.93
Chiller R	-1.00	-0.97	10.81	-5.66	-3.06	2.15
Box Air	18.28	18.33	20.65	18.62	20.53	20.51
Y11	20.63	20.73	22.68	21.41	20.90	22.70
X10	22.34	22.44	24.15	23.29	22.60	24.10
X5	21.68	21.75	23.44	22.78	27.86	23.37
X4	22.85	22.97	21.49	24.08	23.97	24.54
Y3	20.70	20.80	22.31	21.61	21.05	22.53
Temp (C)						
Time	7/18 - 09:51	7/18 - 17:20	7/19 - 10:14	7/19 - 15:39	7/20 - 13:35	7/20 - 18:06
DP	-17.99	-18.28	-18.25	-19.00	-21.12	-21.23
DTU	-5.00	-5.44	-5.20	-5.29	-4.98	-4.83
CP	-17.40	-17.55	-16.99	-17.16	-13.23	-18.83
Chiller S	-5.05	-5.03	-5.03	-5.05	-4.91	-4.91
Chiller R	-3.30	-3.26	-3.30	-3.33	-3.18	-3.18
Box Air	18.23	18.23	18.26	18.09	18.04	17.97
Y11	20.80	20.87	20.90	20.75	20.78	20.70
X10	22.58	22.66	22.66	22.51	22.48	22.41
X5	22.05	22.05	22.12	21.92	21.92	21.90
X4	23.29	23.32	23.34	23.19	23.19	23.15
Y3	21.05	21.12	21.14	20.97	21.00	20.92

Table 5-2 – Temperature data for the beam test in July and August of 2006. DP (Dew Point), DUT (Detector Under Test), CP (Cold Plate: aluminum plate where are located the Peltier Cells that cool down the detector), Chiller S (Chiller Supply: temperature of the coolant at the entry point), Chiller R: (Chiller Return: temperature of the coolant at the exit point), Box air is the air temperature inside the telescope. Y11, X10, X5, X4 and Y3 correspond with the temperatures of the BTeV detectors. Due to technical problems we were not able to monitor the temperature of 1 BTeV detector (X9).

Temp (C)						
Time	7/21 – 12:34	7/24 - 14:00	7/24 - 19:30	7/25 - 10:35	7/26 - 08:00	7/27 - 07:45
DP	-21.03	-13.30	-13.28	-13.28	-9.54	-13.51
DTU	-4.59	5.45	5.43	5.45	17.31	7.08
CP	-18.76	-3.96	3.96	-3.96	14.27	2.12
Chiller S	-4.74	-6.38	6.38	-6.38	25.82	8.38
Chiller R	-2.96	-4.76	-4.74	-4.74	25.28	9.18
Box Air	18.43	18.18	18.18	18.18	20.58	23.02
Y11	21.14	20.56	20.56	20.96	20.85	23.44
X10	22.90	22.27	22.29	22.29	21.49	24.27
X5	22.44	21.92	21.92	21.92	20.24	23.54
X4	23.66	23.12	23.15	23.15	21.07	24.54
Y3	21.41	20.90	20.95	20.95	20.83	24.67
Temp (C)						
Time	8/12 – 15:04	8/13 - 08:32	8/13 - 12:15	8/14 - 08:44	8/14 - 12:25	8/15 - 12:04
DP	-11.77	-12.09	-13.07	-12.44	-12.70	-16.70
DTU	-1.77	-1.65	-1.90	-2.08	-2.19	-1.62
CP	-24.42	-24.47	-24.42	-24.78	-24.83	-24.44
Chiller S	-5.95	-5.71	-5.97	-5.97	-6.00	-5.54
Chiller R	-3.88	-3.59	-3.91	-3.94	-3.94	-3.44
Box Air	17.83	21.03	17.75	20.01	17.75	18.22
Y11	21.11	21.89	20.94	20.80	20.70	21.85
X10	21.86	22.82	21.74	21.57	21.43	22.82
X5	22.25	23.30	22.13	21.98	21.81	23.23
X4	22.75	23.83	22.65	22.48	22.31	23.13
Y3	21.73	21.73	20.98	20.71	20.66	21.73

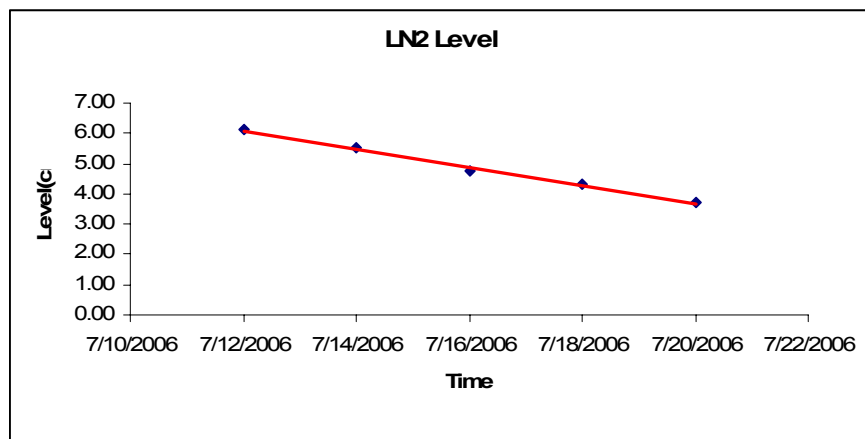


Figure 5-1. Nitrogen Level vs. Time. This was used to study the nitrogen decay rate and then to estimate the day that a new nitrogen cylinder had to be ordered.

Table 5-3 - Nitrogen Level at the test beam for the CMS Fpix detector in July and August of 2006. NI (Nitrogen Information), DL (Dewar Level) and fm (flow meter).

Date	DL(cm)	Left fm	Right fm	Date	DL(cm)	Left fm	Right fm
7/12 - 16:30	6.10	0.0	7.0	7/19 - 15:39	3.60	2.0	5.0
7/13 - 09:26	5.70	0.0	7.3	7/20 - 13:35	3.70	1.8	7.0
7/13 - 15:57	5.15	0.0	7.0	7/20 - 18:06	3.70	2.0	8.0
7/13 - 20:00	5.15	0.0	7.0	7/21 - 12:34	3.60	2.0	7.5
7/14 - NR	5.50	0.0	7.5	7/24 - 14:00	2.42	0.0	5.0
7/14 - 15:00	5.50	0.0	7.0	7/24 - 19:30	2.50	0.0	5.0
7/15 - 09:00	5.50	2.0	6.0	7/25 - 10:35	2.18	0.0	5.0
7/15 - 15:20	5.07	2.0	6.0	7/26 - 08:00	2.00	0.0	4.0
7/16 - 09:15	4.76	2.0	6.0	7/27 - 07:45	NR	0.0	4.0
7/16 - 15:20	4.76	2.0	6.0	8/12 - 15:04	2.81	0.5	6.0
7/17 - 09:38	4.60	2.0	6.0	8/13 - 08:32	2.81	0.5	6.5
7/17 - 15:17	4.10	2.0	6.0	8/13 - 12:15	2.81	0.5	6.5
7/18 - 09:51	3.90	2.0	6.0	8/14 - 08:44	2.81	0.5	6.5
7/18 - 17:20	4.30	2.0	6.0	8/14 - 12:25	2.57	0.6	6.5
7/19 - 10:14	3.90	2.0	5.5	8/15 - 12:04	2.50	0.0	0.6

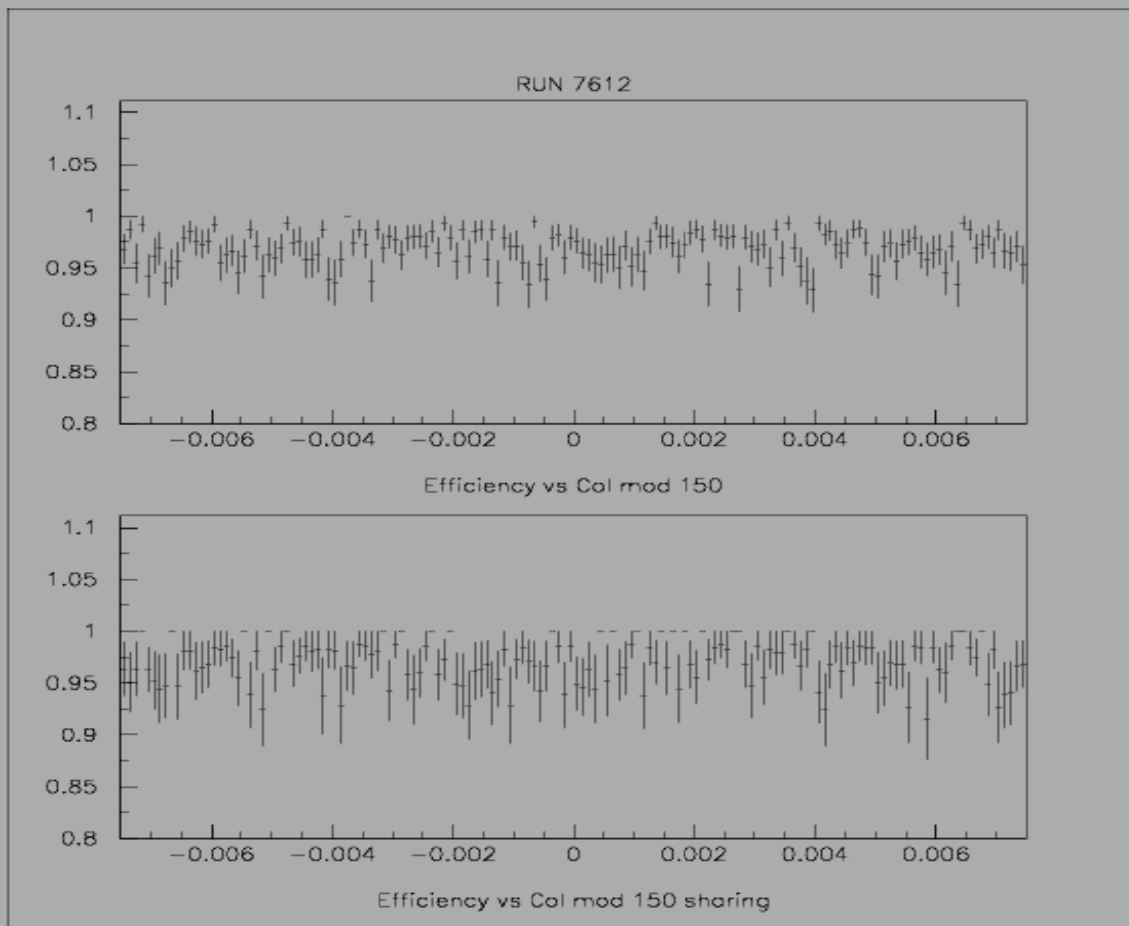


Figure 5-2. Efficiency study for different pixels of an irradiated detector.

The results of the beam test of July-August are not ready yet. Table 5-4 presents some of the data that is being analyzed.

Table 5-4 – Examples of run conditions during some tests of a non irradiated production plaquette. T(Temperature), Vbias(Bias Voltage), Angle is the incidence angle.

August RUN: (2x4 type, P2x4Twp05Cv2 RTI ) Irradiated Plaquette $8 \times 10^{14}$ Beam centered on cell 24				
Run #	Events (M)	T	Vbias	Angle
8510	3.2	-1.3	500	0
8511	NR	-1.7	500	0
8512	3.5	-1.7	500	0
8520	3.2	-1.9	500	0
8522	1	-1.9	500	0
8523	2	-1.86	500	0
<b>Change Vbias to 450 V</b>				
8524	2.3	-1.88	450	0
8525	1.9	-1.9	450	0
<b>Change Vbias to 400 V</b>				
8526	1.4	-1.95	400	0
8527	3.4	-1.77	400	0
<b>Change Vbias to 350 V</b>				
8529	2.5	-2.08	350	0
8531	0.8	-2.08	350	0
<b>Change Vbias to 300 V</b>				
8532	0.96	-2.08	300	0
8537	1.26	-2.17	300	0

## 5.2 C.A.E.N. SY2527 Power Supply Test and MSC Cable

### 5.2.1 Low voltage results

#### 5.2.1.1 Basic behavior of the power supply

Figure 5-3 shows the part of the circuit that was active during this test. Changing the load in the circuit ( $R_L$ ) and doing the measurement of current (IMon) for a fixed nominal voltage, we tested the basic behavior of the power supply using the CDF cable. We used three different loads in the circuit of 1.1, 0.55 and 0.38  $\Omega$ . To compensate for the voltage drop in the cable resistance,

the power supply has an output voltage which is higher than the required value at the circuit (nominal voltage,  $V_N$ ). This voltage value at the power supply is called the driving voltage ( $V_D$ ).

The driving voltage was one of the values that was measured to determine whether the power supply maintained the correct nominal voltage and to measure the resistance of the cable. Figure 5-4 is a set of graphs of the driving voltage versus the current for different nominal voltages. As we expected, the graph for a given nominal voltage is linear and the slope is the same for different values of nominal voltage, since  $R_c$  and  $R_L$  are materials that satisfy Ohm's law. Physically the slope is the cable resistance  $R_c$ .

Mathematically:

$$i = \frac{V_N}{R_L} \quad (2)$$

explains how we varied  $i$  by varying  $R_L$  while maintaining  $V_N$  fixed.

We verified the following relationship experimentally:

$$V_D = V_N + iR_c \quad (3)$$

By measuring the slope we determined  $R_c = 0.5\Omega$ . By determining the intercept of these lines on the vertical axis, we measured values of  $V_N$  that coincided with the set nominal value within the experimental error thus verifying the performance of the power supply. Although a resistance measurement might seem to be trivial, we did not have at hand an ohmmeter that could be used to directly measure such low resistances with precision.

For the MSC cable we did the same measurement for nominal voltages of 2.5V and 1.75V, as is shown in Figure 5-5. These are the operating voltages of the pixel detector electronics. According to the manual of the power supply, the maximum value of current with a voltage of 2.5V is 13A and for 1.25 is 6A [9]. We tested the behavior of the power supply with

currents up to 12.75A for 2.5 V and 5.80A for 1.75 V without problem and these confirmed the values in the manual.

As can be seen from Figure 5-5, the slope (resistance) for the 1.75V points is different from that of the 2.5V. This corresponds to the fact that we used two wires in series (each 0.2  $\Omega$ ) to make the 1.75V connection while we used two pairs of wires in parallel to make the 2.5V connection. Therefore the theoretical cable resistances were 0.4 $\Omega$  for the 1.75V case and 0.2 $\Omega$  for the 2.5V. From the slopes of the graphs we measured resistances of  $R_c = 0.41\Omega$  for 1.75V and  $R_c = 0.21\Omega$  for 2.5V which are totally consistent with the manufacturer's specification.

We also measured the value of capacitance between the different wires of the MSC prototype. The results are shown in Table 5-5.

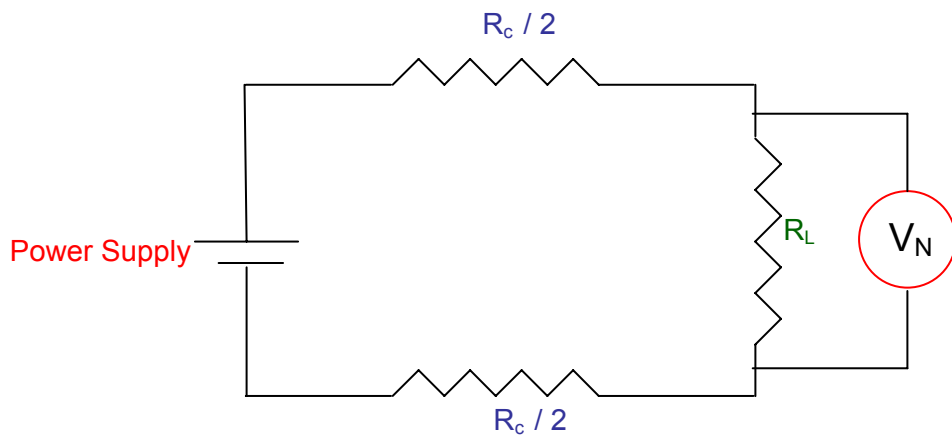


Figure 5-3. Active part of the circuit during the study of the basic behavior of the power supply.  $R_c$  is the cable resistance and  $R_L$  is the load resistance.



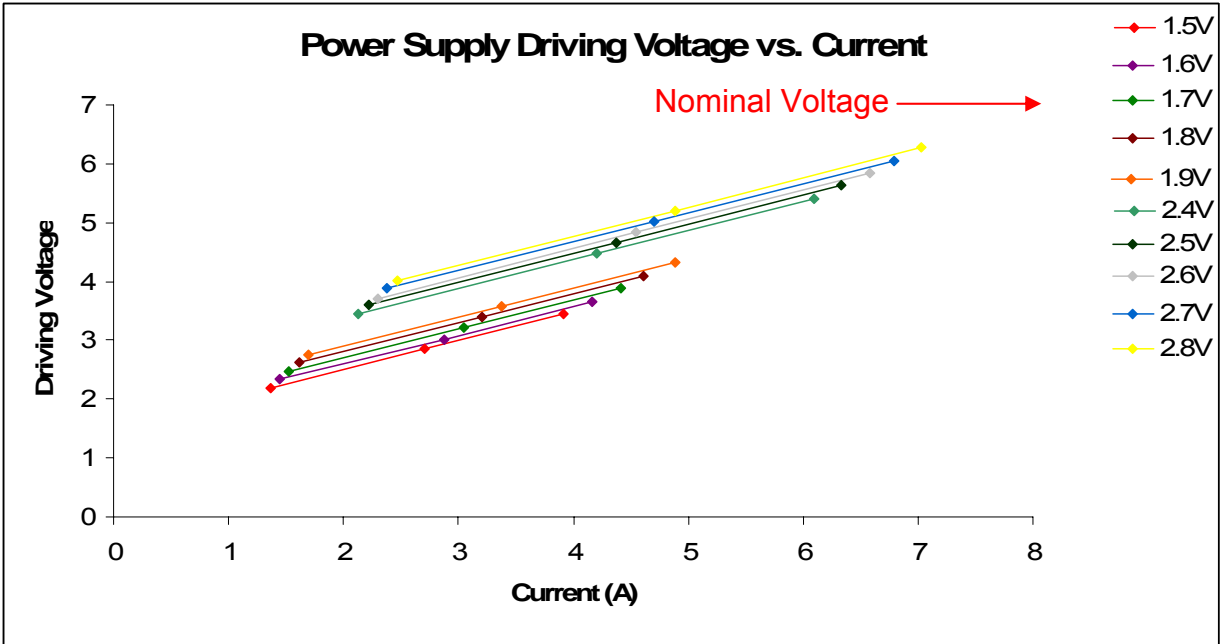


Figure 5-4. The slope is the resistance of the CDF cable and the intercept is very close to the nominal voltage.

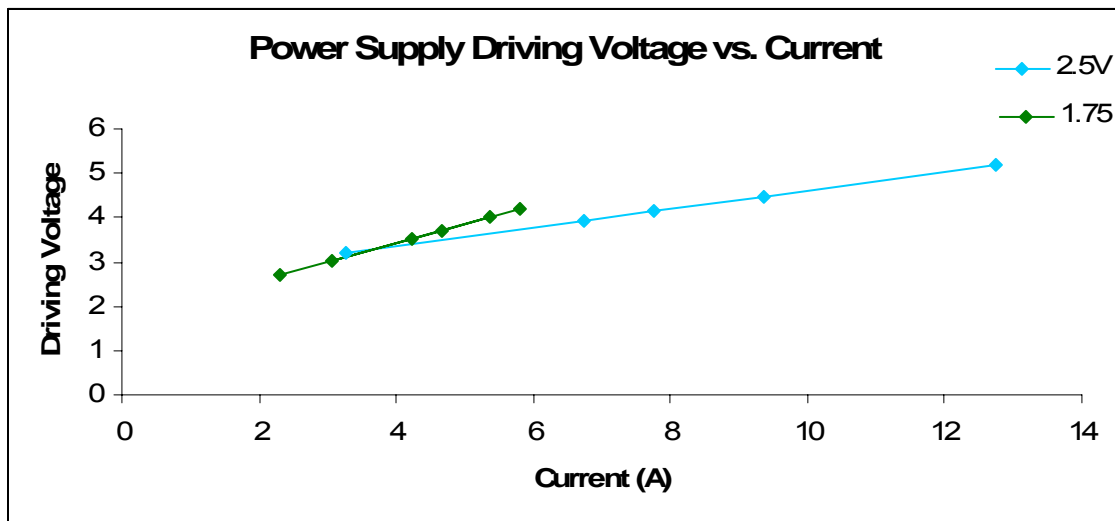


Figure 5-5. Power supply driving voltage versus current for 2.5 and 1.75V nominal voltages, with the MSC cable.

Table 5-5 – Capacitance between the wires of the MSC cable. Su means supply wire and Ret return wire.

Su(2.5V)	Ret(2.5V)	Su(1.75V)	Ret(1.75V)	Sense	HV Su	HV Ret	C(nF)
X	X						14.1
X		X					6.8
X				X			2.8
X					X		2.6
		X	X				6.8
		X		X			2.3
			X		X		2.3
					X	X	8.5

### 5.2.1.2 Power supply response

The oscilloscope was connected as is shown in Figure 4-12 and the numbers 1, 2 and 3 correspond to signals in Figure 5-6. Signal #1 (pink) shows the power supply behavior.

The perturbation (2) is a signal that is applied to the circuit through the FETs and is measured at the resistor that is connected in series to the FETs (Figure 4-12). The input pulse (3) is the signal that comes from the pulse generator to the FETs. As can be seen from this trace, this level changes very quickly, i.e. within a time which is much smaller than the  $20\mu s$  scale of the oscilloscope. In fact the rise time of the generated pulse is 200 ns. On this scale, it seems to occur instantaneously. The perturbation pulse trace shows that the FETs react quickly enough to provide the circuit with a perturbation which is also instantaneous on this scale.

When the perturbation starts, the voltage provided by the power supply drops (sag) since it is not able to react quickly enough to the fast perturbation. After the abrupt change, the perturbation is kept constant for a period of  $100\mu s$  (the width of the pulse). During this time the power supply tries to recover, i.e. return to the nominal voltage. However, this takes a certain amount of time. The power supply is a very complicated device and this recovery does not follow a simple behavior. However, it can be approximated as the sum of two exponentials with

different time constants. Hence, we will speak about a fast recovery time and a slow recovery time corresponding to the two time constants. When the perturbation is over, the power supply voltage has almost returned to the nominal value. (This is not true in all cases as we shall see later.) But again it is unable to react quickly enough to the elimination of the perturbation. It now provides too much voltage (overshoot) and again a process of recovery to the nominal voltage occurs.

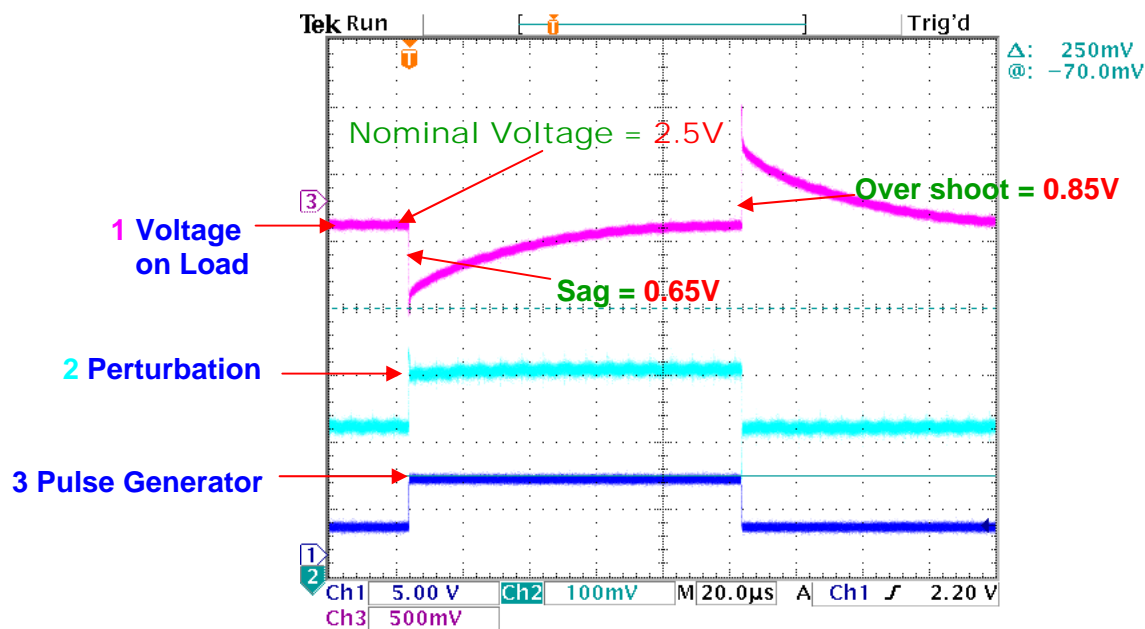


Figure 5-6. Curves for the low voltage test with the C.A.E.N. power supply. The signals are without capacitor and the pulse from the wave generator is 100μs width and has a rise time of 200ns.

Several tests of the power supply behavior were carried out under different circuit conditions. The load resistance in the circuit was varied by changing the number of load resistors connected in parallel. This, of course, affected the current being drawn from the power supply. This is the circuit current alluded to in the results presented here. The load circuit was also changed by adding different capacitors in parallel with the load resistors. Of course, this did not affect the circuit current but it affected the response to the fast perturbation pulse. Other parameters that were varied were the nominal voltage and the perturbation pulse width.

The power supply is a very complicated device. The objective of this project was to characterize its behavior although it was not expected that we would be able to understand the reasons for all the details of the observed performance.

#### 5.2.1.2.1 Sag

The size of the voltage sag was studied as a function of the circuit current. It was found that the sag decreased as the circuit current increased (Figure 5-7). This can be explained if one considers that the perturbation adds a backward current through the load whose magnitude is independent of the load resistors, i.e. the FETs act as a current generator. It is this additional current which is seen as a sag in the load voltage. Higher circuit currents correspond to lower values of load resistance and thus to lower sag voltages due to the constant perturbation current.

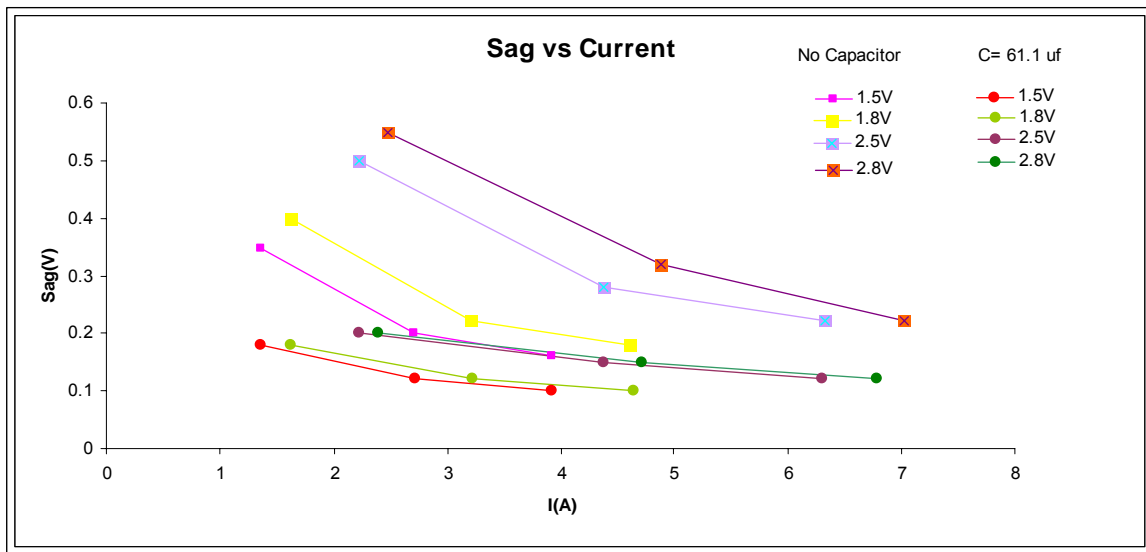


Figure 5-7. Sag vs. Current for different nominal voltages, with and without capacitor.

#### 5.2.1.2.2 Recovery times

Two different recovery times are needed to understand the transient behavior of the power supply. This can be better understood if one analyzes Figure 5-8 which shows only the

voltage supplied to the load. Around  $10\mu s$  after the sag, the exponential recovery rise has almost saturated indicating a time constant smaller than  $10\mu s$ . We call this recovery process the fast process with times of order  $\mu s$ .

However, the voltage has still not returned to its nominal value. This means that there is a component of the recovery which takes much longer to occur. In fact, by studying the recovery after the overshoot and cases with much longer perturbation widths, it is found that the power supply eventually does recover completely but in a time scale of milliseconds.

Figures 5-9 and 5-10 present the results of a study of recovery times versus circuit current. The recovery times were determined by fitting exponentials to the data stored from the oscilloscope trace. Both recovery times increase with increasing circuit current. The fast recovery time seems to have a very linear relationship while the slow recovery time seems to reach a limiting value as the current is increased.

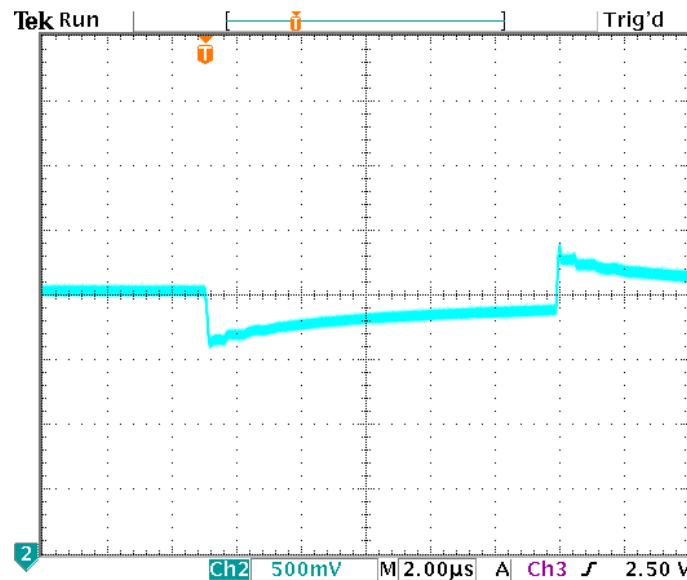


Figure 5-8 Fast and slow recoveries for a circuit without capacitor, nominal voltage of 1.8V and  $11\mu s$  pulse width.

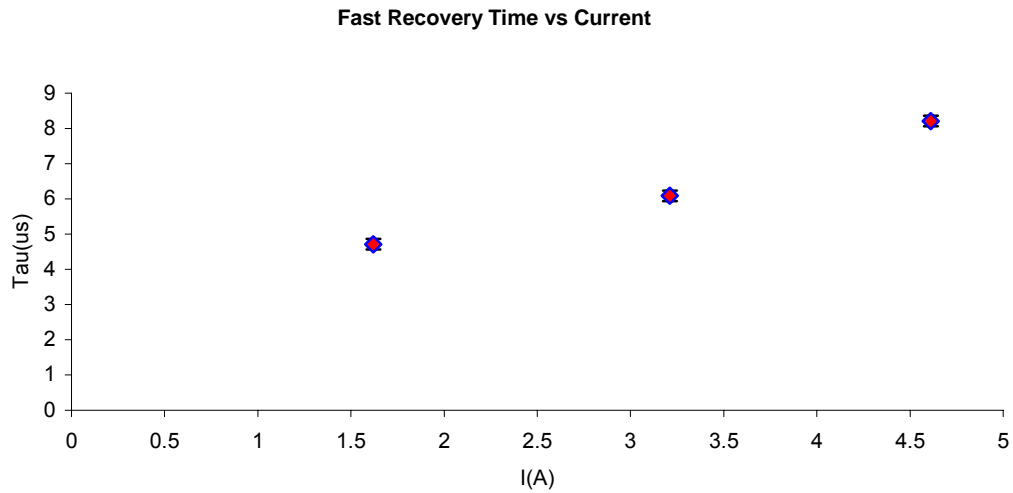


Figure 5-9 Fast recovery times vs current for a circuit without capacitor, nominal voltage of 1.8V and 11 $\mu s$  pulse width.

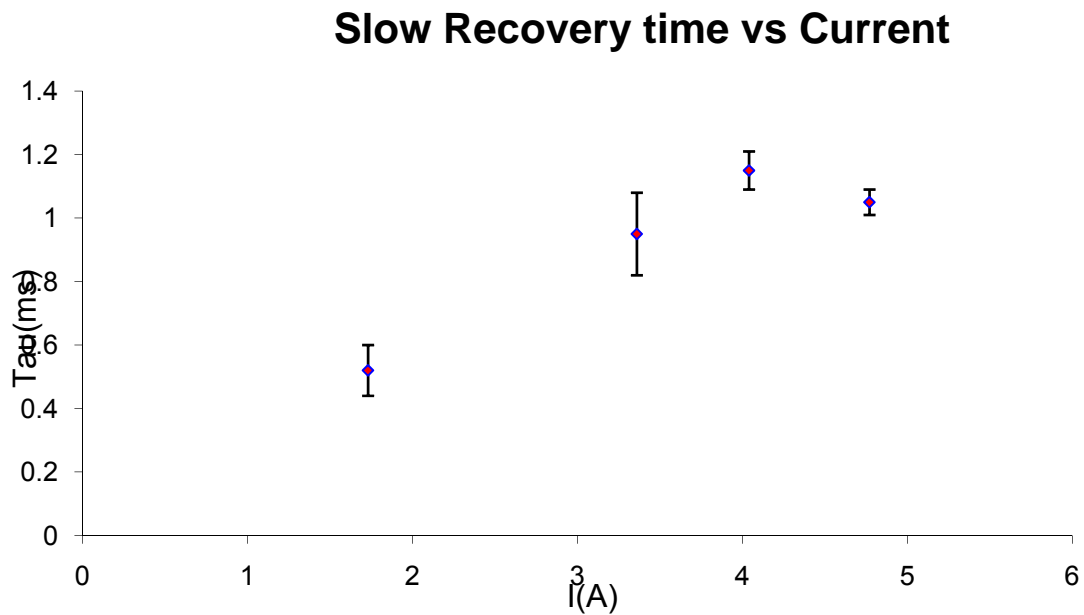


Figure 5-10 Slow recovery time vs current for a circuit without capacitor, nominal voltage of 1.8V and 11 $\mu s$  pulse width.

### 5.2.1.2.3 Signals with capacitor

An external capacitor adding to the internal capacitance of the cable (connected in parallel) gives rise to better filtering of the high frequency components as shown in Figure 5-11.

We tested with different kinds of capacitors (ceramic, electrolytic, tantalum) with similar values of capacitance. The better signals (lower sags) were obtained with the tantalum capacitors.

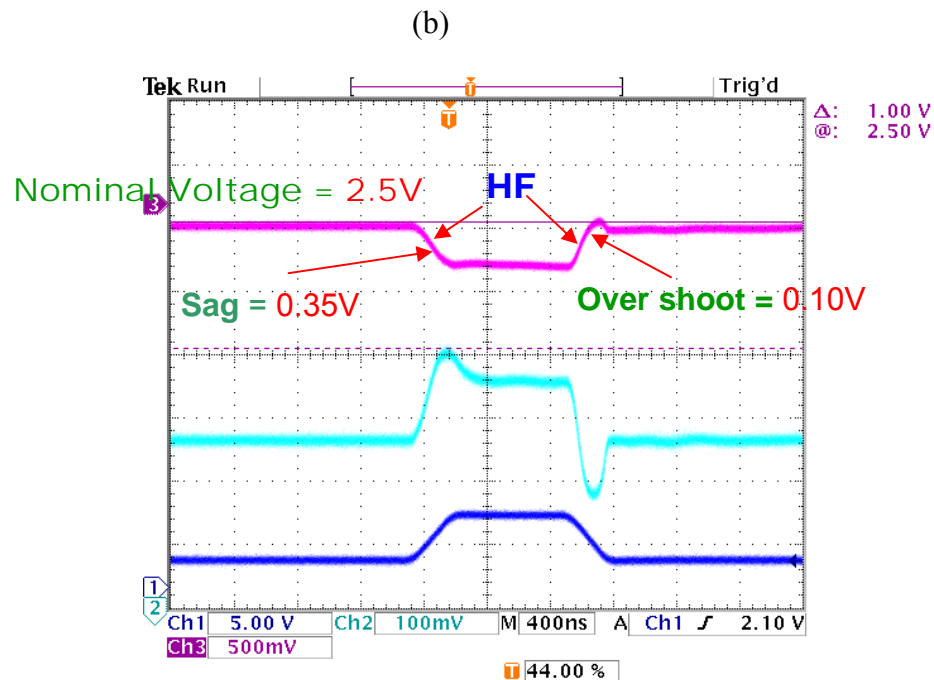
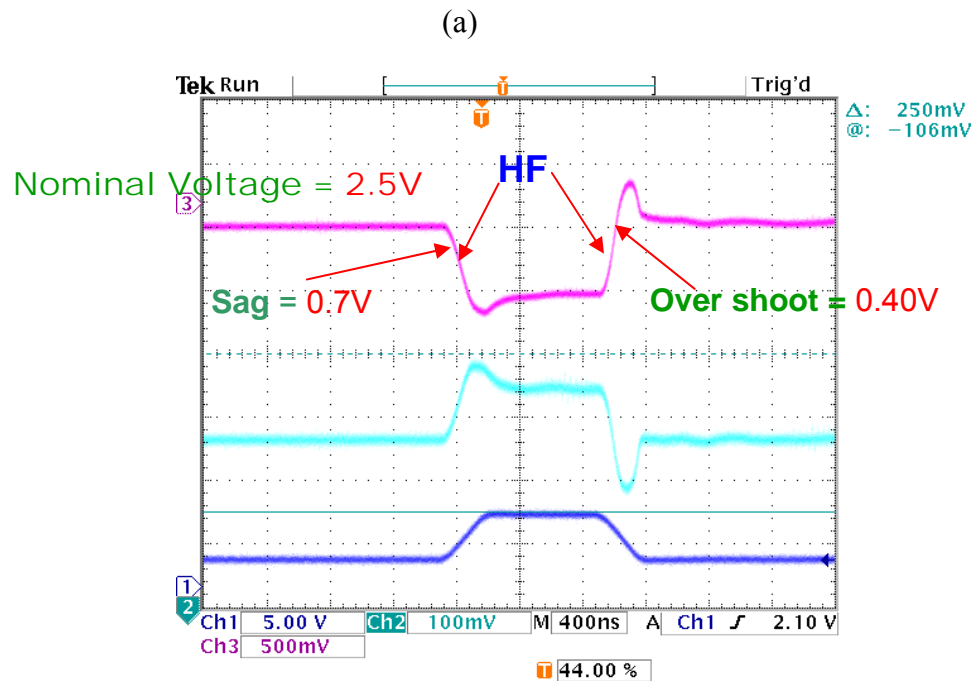


Figure 5-11. a) Signal without capacitor b) signal with capacitor of  $13\mu\text{F}$ . The pulse width in the wave generator is  $1\mu\text{s}$ .

### 5.2.2 High voltage test

For the high voltage test we used the Plaquette IZM1 (1X2). The high voltage connection was made using two wires of the MSC cable with  $14.64\Omega$ . An adapter was built to make the connection between the plaquette and the C.A.E.N. power supply. Since the photons from a light source also create a signal in the pixels, a box was used to shield the plaquette from light.

In the high voltage test we made a measurement of the leakage current through the pixel sensors as a function of bias voltage. The meter in the power supply can measure a limited range of current in the high voltage regime. It can measure current no lower than  $10\mu\text{A}$  and no larger than  $20\text{mA}$ . The leakage current is of the order of nanoamperes and to measure it we used a picoammeter connected in series with the MSC cable.

This test was carried out at room temperature. The results were compared with previous tests done over one year ago using the “COSMOS” test stand. COSMOS was designed to do plaquette testing using other power supplies and other short cables. We retested using COSMOS both at room temperature and at  $-20^\circ\text{C}$ .

Figure 5-12 presents three graphs of current vs. voltage. It can be noticed that the differences between the curves with COSMOS and those done with the C.A.E.N power supply using the MSC cable are relatively small. The larger difference is with the performance over one year ago. In order to rule out the possibility that the plaquette had been damaged or had degraded during the intervening year, we tested the plaquette at a temperature of  $-20^\circ\text{C}$ . It was found to perform very well with a very small leakage current. The differences between the graphs at room temperature are believed to be due to differences in room temperature.

The four graphs have a linear behavior up to approximately  $180\text{ V}$ . After this value the behavior becomes non-linear which is typical of semiconducting devices.



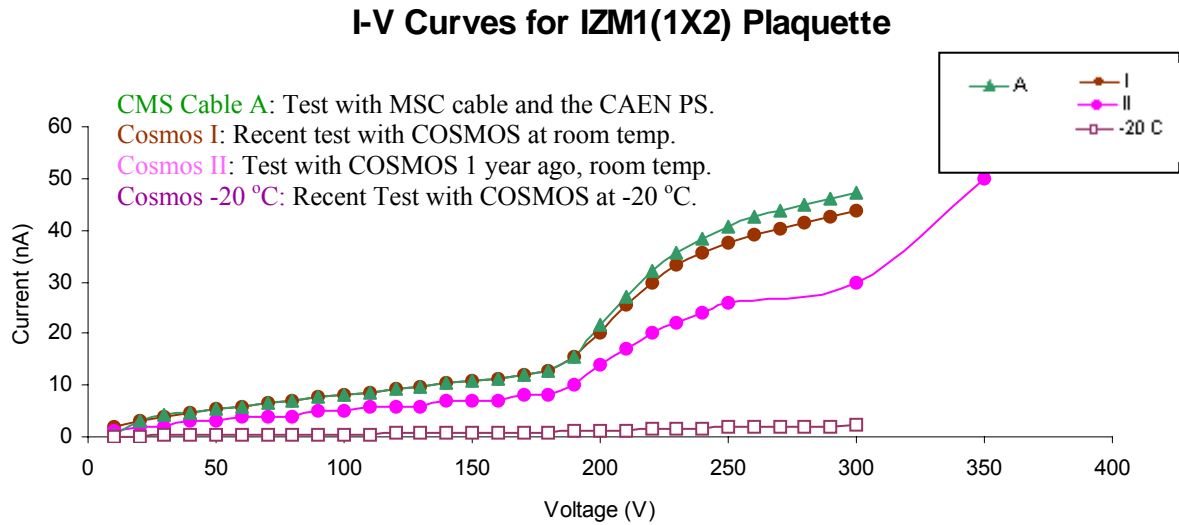


Figure 5-12. High voltage tests with the plaquette IZM1 (1X2).

### 5.2.2.1 Spikes in the low voltage and high voltage output

Spikes with frequencies of 77 KHz and 156 KHz were found in the low voltage and high voltage outputs of the power supply. These spikes come directly from the power supply. The high and low voltage spikes were detected even with the channel turned off. The spikes are shown in Figure 5-13. Table 5-6 shows the results for the measurements with three values of voltage for the high voltage connection. After these results were found by us, a complete study of these spikes was performed by electronic experts. They found that the frequency and voltage of the spikes do not represent a risk for the electronics of the detector.

### 5.2.3 High voltage and low voltage at the same time

In the previous tests we tested the high voltage and low voltage separately. In the actual experiment both levels of voltages will be working at the same time. Thus, it is necessary to test the behavior of the power supply in this condition.

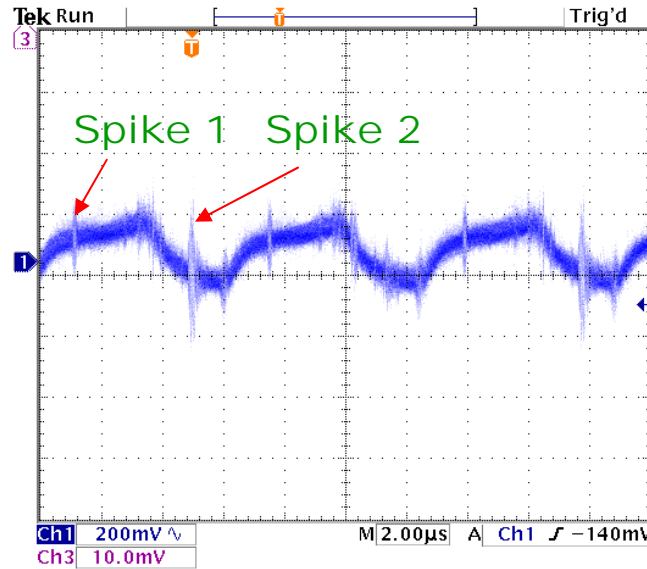


Figure 5-13. Spikes in the low voltage and high voltage power supply output.

Table 5-6 – Results for the spikes in the HV channel of the power supply. (NV) Nominal voltage, (Vs1) Voltage spike 1, (Vs2) Voltage spike 2, (F1) Frequency of spike 1, (F2) Frequency of spike 2

Nv (V)	Vs1 (V)	Vs2 (V)	F1 (KHZ)	F2 (KHZ)
None	0.12	0.13	156.25	76.92
100	0.12	0.20	156.25	76.92
290	0.12	0.23	156.25	76.92

Two different kinds of circuits were used for this test. The first one was the dynamic circuit that was used to test the power supply behavior with the low voltage as described in section 4.2.3. The second were static circuits with resistors of  $1\text{M}\Omega$  and  $1.2\Omega$  to make independent connections of high voltage and low voltage. We connected two low voltages and one high voltage from one PS channel simultaneously (Figure 5-14). We used the CMS cable.

Power Supply

100 V

2.5 V

1.75 V

Dynamic circuit

Tek Run Trig'd  
 4  
 2  
 1  
 3  
 Ch1: 500mV  $\Omega$  Ch2: 100mV  
 Ch3: 5.00V Ch4: 1.00V  
 M 20.0 $\mu$ s A Ch3: 2.50V  
 10.40%

67

## 5.3 Test Stand for the Partial Forward Pixel Detector

### 5.3.1 Cooling test and leakage current measurement

A cooling test was performed for the first pilot-run half-disk of the Fpix detector. We recorded information of temperatures and leakage currents of each panel. The results for these measurements are shown in Figure 5-16.

The results for RTD 1, 3 and 4 are very consistent. Due to a bad thermal contact with the panel surface, RTD2 has an offset with respect to the other three RTDs. After these results were seen, RTD 2 was placed correctly on the panel.

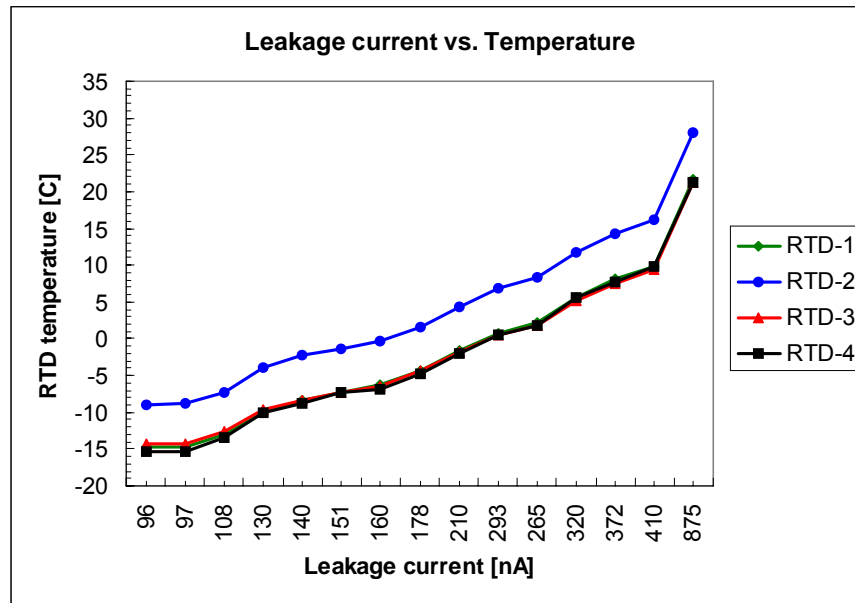


Figure 5-16. Temperature vs. leakage current for each panel on the first half-disk of the Fpix detector.

Using equation 4 [16] that relates the leakage current with temperature for a semiconducting junction, we fit the data from panel1 (RTD1) as is shown in Figure 5-17.

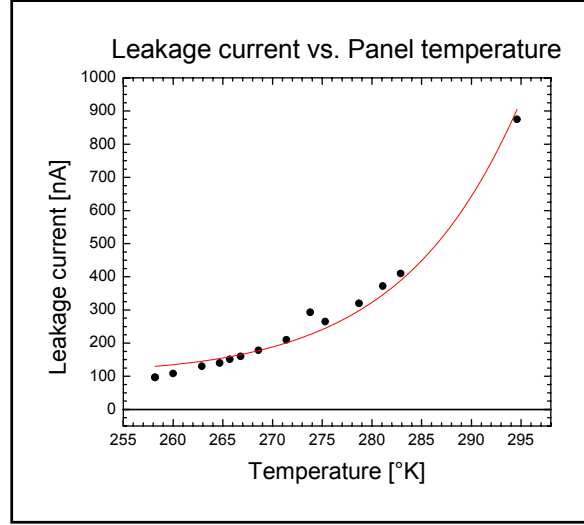


Figure 5-17. Fit for the leakage current on panel1 as a function of temperature.

$$I(T) = I_0 + AT^{3/2} \exp\left(\frac{E_g(T)}{2k_b T}\right) \quad (4)$$

Where [17]

$$E_g(T) = E_g(0) - \frac{\alpha T^2}{T + \beta} \quad (5)$$

$$I_0 = 107 \text{ nA}$$

$$A = 674 \frac{\text{nA}}{\text{K}^{3/2}}$$

$$E_g = 1.17 \text{ eV}$$

$$\alpha = 4.73 \times 10^{-4} \frac{\text{eV}}{\text{K}}$$

$$\beta = 636 \text{ K}$$

These results confirm that the device behaves as expected.

### 5.3.2 Half-service-cylinder Cold Box

After cooling and humidity tests were performed on the half-service-cylinder cold box, it was necessary to perform several modifications to meet the required standards. Four extra loops of cooling lines of a bigger diameter were installed in order to reach the run temperature of

-20°C. Due to moisture in the wood of the box, the humidity level was too high. To reach the necessary humidity level, the internal walls of the cold box were shielded with aluminum foil.

## 5.4 DCS to FEC Interface

### 5.4.1 Interface Status

With respect to the task list presented in section 4.4, the status of the PixelDCStoTrkFECdpInterface implementation is the following:

1. The access of the PixelDCStoTrkFECdpInterface to the Configuration database, the retrieval of the calibration parameters and names of the PVSS data points has been implemented. As the final format of the Configuration database tables is not defined yet, a set of dummy tables is used now. Upon clicking on the PixelDCStoTrkFECdpInterface icon shown in Figure 4-21, a new web page will be displayed as in Figure 5-18. In this new web page the password to access the Configuration database has to be entered. For use in the actual experiment this manual entering of the password has to be replaced by another mechanism.

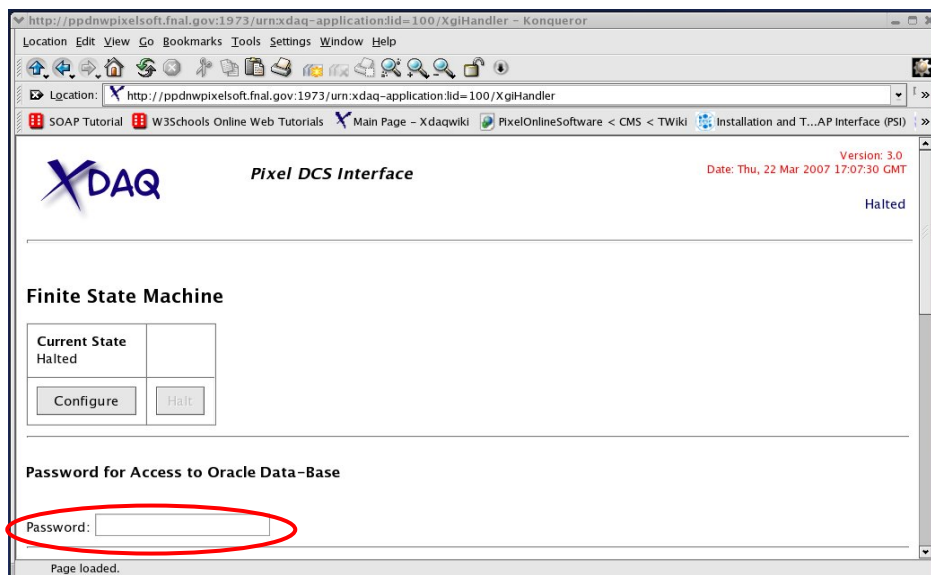


Figure 5-18. View upper half part of the PixelDCStoTrkFECdpInterface browser.

2. After the Configuration database has been accessed; the test application, PixelDCSMessage, sends a SOAP message containing three data point values to the PixelDCStoTrkFECDpInterface. The message is shown in Figure 5-19. The PixelDCStoTrkFECDpInterface decodes the message. Some debug output of the decoding is shown in Figure 5-20 where the number of body elements, the number of child elements, and the attribute names with their corresponding attribute values are shown.
3. The interface then transforms the raw ADC values into temperatures. For testing purposes a dummy transformation formula is used at present. Then the running average is calculated for each channel using formula (1).

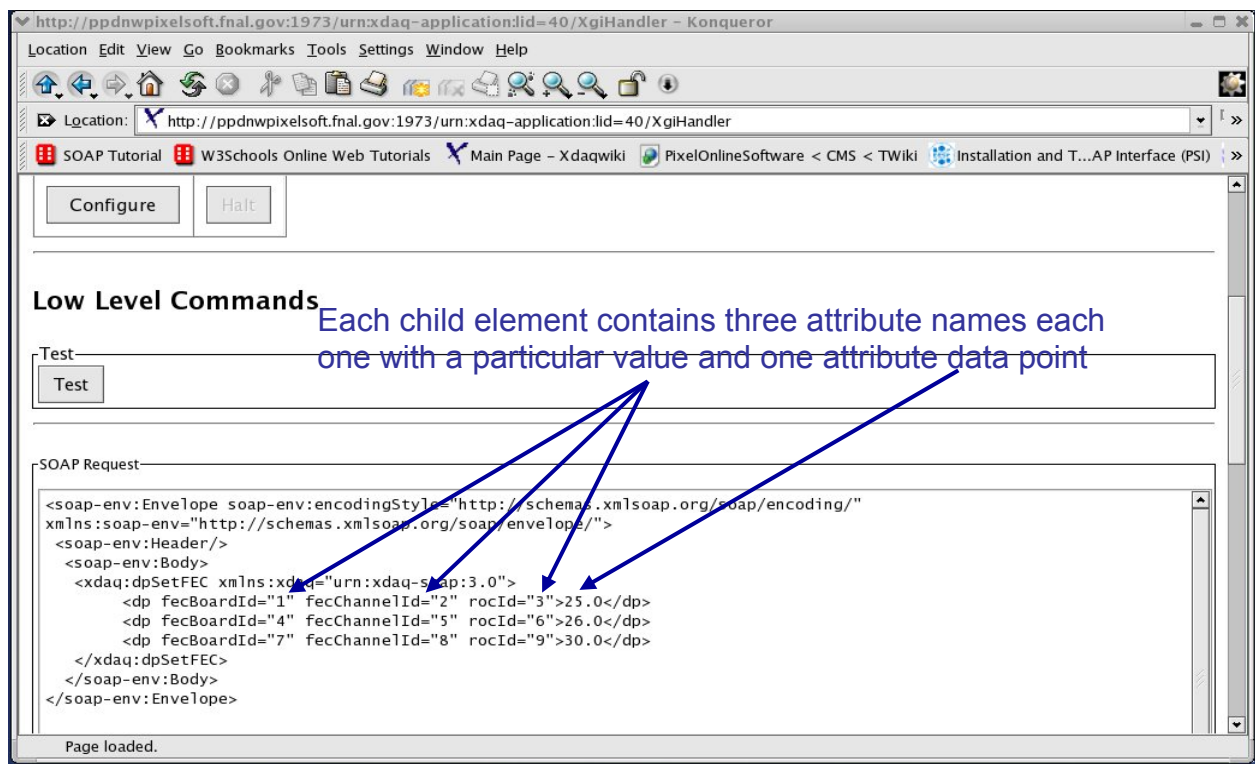


Figure 5-19. Message sent from PixelDCSMessage to test the PixelDCStoTrkFECDpInterface. This message contains three child elements each one with three attribute names each with its own attribute value and one data point attribute value.

```

flores@ppdnwpixelsoft:~/DAQKit/TriDAS/pixel/PixelRun - Shell - Konsole
Session Edit View Bookmarks Settings Help

sportHTTP.lid(1) <> - Header: [host], value: ppdnwpixelsoft.fnal.gov:1973
27 Mar 2007 22:06:1175054799 [3044903856] DEBUG gov.fnal.ppdnwpixelsoft.PeerTran
sportHTTP.lid(1) <> - Header: [content-type], value: multipart/form-data; bounda
ry=-----Atma2SBVhpmBD8wdFNhL45OZVGb9AbBITvqV0zy3miEzoAc4WINYLN
27 Mar 2007 22:06:1175054799 [3044903856] DEBUG gov.fnal.ppdnwpixelsoft.PeerTran
sportHTTP.lid(1) <> - Header: [content-length], value: 194
27 Mar 2007 22:06:1175054799 [3044903856] DEBUG gov.fnal.ppdnwpixelsoft.PeerTran
sportHTTP.lid(1) <> - Mozilla/5.0 (compatible; Konqueror/3.1; Linux)
<PixelDCSMessage::Test>
<PixelDCStoTrkFECdpInterface::dpSetFEC>
Number of BodyElements = 1
  BodyElement name = xdaq:dpSetFEC
  Number of ChildElements = 3
    ChildElement name = dp
    'Board Id '1' Value for FEC channel '2', roc '3' set to '25'.
    ChildElement name = dp
    'Board Id '4' Value for FEC channel '5', roc '6' set to '26'.
    ChildElement name = dp
    'Board Id '7' Value for FEC channel '8', roc '9' set to '30'.
Sending SOAP request to URL = http://cannes.fnal.gov:1972
Request : -----
<soap-env:Envelope soap-env:encodingStyle="http://schemas.xmlsoap.org/soap/encod
ing/" xmlns:soap-env="http://schemas.xmlsoap.org/soap/envelope/"><soap-env:Heade

```

Figure 5-20. Debug output generated by the decoding of the SOAP message received from the PixelDCSMessage test application.

4. The interface then applies a dead band condition to determine whether the data point value needs to be updated in PVSS. It is updated only if the running average computed differs by more than 5% with respect to the value stored in PVSS.
5. The dead band check is done for every channel but the actual passing of the updated values is done in a single SOAP message after all the checks are finished in order to avoid the large overhead of repeated SOAP messages.
6. The updated values are then stored in the conditions database.
7. For testing purposes, status information is displayed on a dynamic table with the following parameters:
  - Last data point ID (FecBoard Id, FecChannel Id, roc Id).

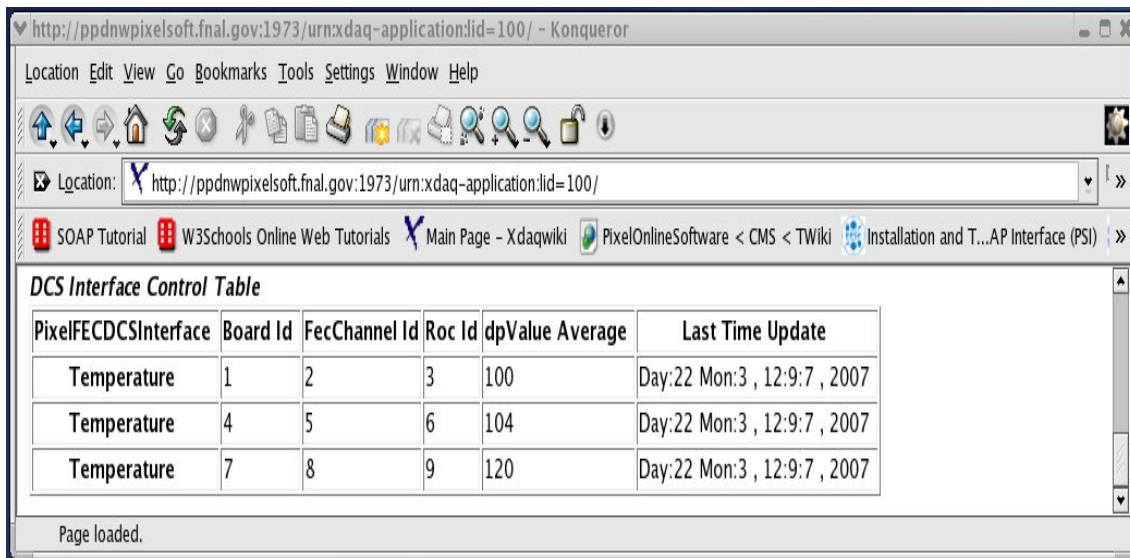


- Running average of temperature value.
- Last time that the PVSS data point corresponding to that channel was updated.

The table is shown in Figure 5-21 and corresponds to the lower half of the PixelDCStoTrkFECDpInterface webpage.

The first version of the PixelDCStoTrkFECDpInterface interface was developed and uploaded to the CVS repository. The CVS repository is the storage for the official versions of all CMS software. All CMS collaborators have access to use the software developed by others and to submit their own software. It is an important facility to monitor and control the enormous amount of CMS software so that there is uniformity and compatibility among the various components of this software. It can be found at:

<http://issecvs.cern.ch/cgi-bin/cvsweb.cgi/TriDAS/pixel/PixelDCSInterface/?cvsroot=tridas>



Page loaded.

PixelFECDCSInterface	Board Id	FecChannel Id	Roc Id	dpValue Average	Last Time Update
Temperature	1	2	3	100	Day:22 Mon:3 , 12:9:7 , 2007
Temperature	4	5	6	104	Day:22 Mon:3 , 12:9:7 , 2007
Temperature	7	8	9	120	Day:22 Mon:3 , 12:9:7 , 2007

Figure 5-21. Lower half of the webpage displayed by PixelDCStoTrkFECDpInterface application.

## **Chapter 6 - Summary and Conclusions**

### **6.1 Forward Pixel Beam Test**

- A. The DCS and the SMC for the test of the CMS Fpix detector were installed in the Meson Test facility at Fermilab.
- B. Temperatures and humidity were monitored during the test.
- C. The detectors did not overheat and no overcurrent or humid air condensation was registered.
- D. Irradiated plaquettes worked well and do not present a significant damage in the January 2006 test.
- E. The plaquette efficiency was almost 100%.

### **6.2 C.A.E.N. SY2527 Power Supply and MSC Cable**

We performed a complete study of the low voltage and high voltage channels of the C.A.E.N power supply.

- A. Low voltage channel
  - 1. The PS provided the correct nominal voltage.
  - 2. We reached values of current close to the specified limits for the A4603 HV/LV module for the two low voltages tested.
  - 3. The measured properties of the MCS cable prototype matched the specifications of the manufacturer.
  - 4. The transient response of the PS was studied and characterized. It was found to depend on the characteristics of the circuit. In general, for very

fast perturbations, there is a sag in the output voltage with a double exponential time recovery.

5. The sag decreases with increasing current.
6. The sag decreases with increasing capacitance.
7. The response time increases with increasing current.

B. High Voltage Channel

1. The differences between the results obtained with the COSMOS setup and the C.A.E.N power supply using the MSC cable are relatively small.
2. There is a small difference with the performance of a year ago. This could be due to a difference in room temperature.
3. The high and low voltage signals have spikes even with the channel turned off. The amplitude and frequency of the spikes do not represent a risk for the electronics.

### **6.3 Test Stand for the Partial Forward Pixel Detector**

- A. The half-disk test stand for the testing of the CMS Fpix pilot run detector was assembled.
- B. The cold box test stand for the half-service-cylinder was assembled. The cooling and humidity tests for the half-disk and half-service-cylinder test stands were performed.
- C. The cold box for the half-service-cylinder was shielded with aluminum.

- D. The partial detector project is permitting us to identify problems and develop solutions which we will use when the full detector is being assembled.

## **6.4 DCS to FEC interface Software**

The first version of the software interface for the data collection of ROC temperatures was written. It moves the data from the FEC to the PVSS system.

- A. The code for the interface is in the CVS repository.
- B. A test application to check the interface was developed.

## References

- [1] G. Bruno, Brief Survey with CMS in Year One, arXiv:hep-ex/0308003 v3, 2003.
- [2] CERN DSU-Communication Group, LHC Machine Outreach, <http://lhc-machine-outreach.web.cern.ch/lhc-machine-outreach/>, 2006.
- [3] CMS Collaboration, *Physics Technical Design Report, Detector Performance and Software*, Vol1, CERN, p.7-23, 2006.
- [4] G. Lutz, *Semiconductor Radiation Detectors*, Springer-Verlag Berlin Publishing Company, Heidelberg, Chapter 3, 1999.
- [5] CMS Collaboration, *Technical Design Report, The Tracker Project*, Vol1, CERN, p. 14-19, 1998.
- [6] D. Kotlinski, The Control and Readout System of the CMS Pixel Barrel Detector, *Nucl. Instrum. Methods A* 565, p. 73, 2006.
- [7] J. Butler, Pixel Detector, [http://home.fnal.gov/~florez/NIM\\_Pixel\\_section.pdf](http://home.fnal.gov/~florez/NIM_Pixel_section.pdf), 2007.
- [8] JC Electronica, Thermoelectric Cooling with Peltier Cells, <http://www.jcelectronica.com/articles/peltier.htm>, 2007.
- [9] CAEN, SY2527 User's Manual, <http://www.caen.it/getattach.php?mod=SY2527&obj=mn&id=1419>, 2005.
- [10] D. Menasce, L. Uplegger and M. Turquetti, The Renaissance: a test-stand for the Forward CMS Pixel Tracker assembly. <http://home.fnal.gov/~florez/Renaissance.pdf>, 2007.
- [11] M. Eads, Assembly, Testing, and Performance of the CMS Forward Pixel Detector Modules, [http://home.fnal.gov/~florez/paper\\_eads.pdf](http://home.fnal.gov/~florez/paper_eads.pdf), 2007.
- [12] [http://xdaqwiki.cern.ch/index.php/Main\\_Page](http://xdaqwiki.cern.ch/index.php/Main_Page)
- [13] W3 Schools, Soap Tutorial. <http://www.w3schools.com/soap/default.asp>, 2002.
- [14] W3 Schools, Soap Tutorial. [http://www.w3schools.com/xml/xml\\_attributes.asp](http://www.w3schools.com/xml/xml_attributes.asp), 2002.
- [15] H. C. Kastli, Design and Performance of the CMS Pixel Readout Chip, *Proceedings of the Eighth Workshop on Electronics for LHC Experiments*, <http://lhc-electronics-workshop.web.cern.ch/LHC-electronics-workshop/2002/home.htm>, 2002.
- [16] M. Shur. *Introduction to Electronic Devices*. J. Wiley & Sons Publishing Company. p. 208, 1996.

[17] B. Van Zeghbroeck, Principles of Semiconductor Devices, <http://ece.colorado.edu/~bart/book/eband5.htm>, 2004.